Civil Engineering Faculty Publications and Presentations

Department of Civil Engineering

Double Averaging Analysis Applied to a Large Eddy Simulation of Coupled Turbulent Overlying and Porewater Flow

Yan Ping Lian
Beijing Institute of Technology

Jonathan Dallman
Northwestern University

Benjamin Sonin
Northwestern University

Kevin R. Roche
Boise State University

Aaron I. Packman
Northwestern University

See next page for additional authors

Authors

Yan Ping Lian, Jonathan Dallman, Benjamin Sonin, Kevin R. Roche, Aaron I. Packman, Wing Kam Liu, and Gregory J. Wagner

Correspondence to:
J. Dallmann,
jonathan.dallmann2020@u.northwestern.edu

Double Averaging Analysis Applied to a Large Eddy Simulation of Coupled Turbulent Overlying and Porewater Flow

Yan Ping Lian[1], Jonathan Dallmann[2,3], Benjamin Sonin[2], Kevin R. Roche[4], Aaron I. Packman[2,5], Wing Kam Liu[2], and Gregory J. Wagner[2]

[1]Institute of Advanced Structure Technology and State Key Laboratory of Explosion Science and Technology, Beijing Institute of Technology, Beijing, China, [2]Department of Mechanical Engineering, Northwestern University, Evanston, IL, USA, [3]Center for Preparatory Studies, Nazarbayev University, Nur-Sultan, Kazakhstan, [4]Department of Civil Engineering, Boise State University, Boise, ID, USA, [5]Department of Civil and Environmental Engineering, Northwestern University, Evanston, IL, USA

Abstract Freestream turbulence in rivers is a key contributor to the flux of dissolved nutrients, carbon, and other ecologically important solutes into porewater. To advance understanding of turbulent hyporheic exchange and porewater transport, we investigate flow over and through a rough bed of spheres using large eddy simulation (LES). We apply double averaging (combined space and time averaging) to the LES results to determine the mean velocity distribution, momentum balance, and drag forces. Our simulations show large-scale freestream structures interacting strongly with vortices generated at the surfaces of individual spheres to control turbulent momentum fluxes into the bed. The transition between turbulent flow and Darcy flow occurs over the first row of spheres, where turbulence decays rapidly and turbulent kinetic energy, Reynolds stress, and drag forces peak. Below this region, turbulence is only present in the high-velocity flow in open pore throats. Experimental observations suggest that minimum mean porewater velocity occurs in the first open pore space below the transition region, but our results show that the minimum occurs between the first and second pore spaces. The simulation mean porewater velocities are approximately half those captured in measurements because the model resolves the entire flow continuum while measurements can access high-velocity fluid in open pores. The high-resolution dual time-space averaging of the LES resolves both turbulent and mean flow features that are important to interfacial solute and particle fluxes, providing a means to include turbulent hyporheic exchange in upscaled river models, which has not been achieved to date.

1. Introduction

Turbulent flow over and through a permeable surface is a common feature of many aquatic systems. Rivers are an important example of such a flow, as they generally have highly turbulent flow over a granular sediment bed. While porewater flow generally decays to Darcy flow deep in the bed, turbulence from the overlying flow penetrates across the sediment-water interface (Blois et al., 2014; Boano et al., 2011; Dade, 2001; Nagaoka & Ohgaki, 1990; Packman et al., 2004; Pokrajac et al., 2007; Roche et al., 2018). This region of exchange between overlying flow and subsurface flow, known as the hyporheic zone, has a dramatic impact on river ecosystems, as hyporheic exchange controls the retention, transformation, and remobilization of nutrients, particulate organic matter, and contaminants (Boano et al., 2014; Jones & Mulholland, 1999; McKnight et al., 2004; Newcomer Johnson et al., 2016; Withers & Jarvie, 2008; Xia et al., 2018).

Early attempts to explore the coupling between overlying flow and porewater flow concentrated on sand beds with large bed roughness features (bedforms; Elliott & Brooks, 1997a; Thibodeaux & Boyle, 1987). Models for these systems treated the subsurface as a homogeneous isotropic porous medium and used Darcy assumptions for hyporheic porewater flow (Elliott & Brooks, 1997b; Packman & Brooks, 2001). For coarse sediment beds, early experimental studies found turbulence played an important role in hyporheic flow (Nagaoka & Ohgaki, 1990; Packman et al., 2004). However, turbulent hyporheic exchange is very difficult to observe experimentally, even in the laboratory, because of obstruction from adjacent bed sediment grains. These limitations have restricted measurements to accessible regions of the bed, either via flow visualization (Packman et al., 2004; Roche et al., 2018) or by measuring velocities in the open pore spaces between

grains (Manes et al., 2009; Pokrajac et al., 2007). More recently, refractive-index-matching techniques have been used to visualize the pore fluid flow more completely (Voermans et al., 2017). Several studies have observed an unexpected velocity minimum in the first pore below the sediment-water interface (Manes et al., 2009; Pokrajac et al., 2007; Roche et al., 2018), and porewater transport has complex patterns that are difficult to reduce into simple expressions such as diffusion coefficients (Roche et al., 2018, 2019). Improved models for turbulent hyporheic exchange are needed, as experimental and numerical investigations have shown that freestream turbulence penetrates into the subsurface (Blois et al., 2012; Kuwata & Suga, 2017; Roche et al., 2018; Shen et al., 2020; Stoesser et al., 2007) and plays a vital role in many of the key functions of the hyporheic zone, such as storage and transformation of stream-borne solutes including nitrogen and organic carbon (Grant, Gomez-Velez, et al., 2018; Jones & Mulholland, 1999; Knapp et al., 2017; Li et al., 2017, 2021).

While great strides have been made in accurately modeling advective hyporheic exchange induced by bedforms in fine-sediment beds (Boano et al., 2014), it has proven difficult to parameterize models for turbulent hyporheic transport based only on fundamental morphological properties and hydrodynamic processes. Most current hyporheic flow models are semi-coupled, meaning that separate solvers are used in the freestream and the bed, linked through boundary conditions imposed at the interface (Boano et al., 2014). Moreover, continuum assumptions are used for the subsurface flow, both the hyporheic zone and the deeper regions of the bed governed by Darcy's Law. For turbulent hyporheic exchange, specification of a problem-specific diffusion coefficient is typical (e.g., Grant, Azizian, et al., 2018; Grant, Gomez-Velez, et al., 2018; Grant et al., 2020; Roche et al., 2018, 2019). These assumptions represent significant shortcomings of available models, as they are unable to directly capture turbulent interactions between surface-fluid and pore-fluid, or turbulent flows in porewaters (Boano et al., 2014; Grant, Gomez-Velez, et al., 2018). The inability to properly resolve turbulence can lead to underestimations of hyporheic exchange by a factor or two or more (O'Connor et al., 2012; O'Connor & Harvey, 2008). Improved understanding of turbulent interactions between surface and porewater is needed along with a method for directly solving both flow regimes and upscaling results into river biogeochemistry models.

Dual spatial and temporal averaging of the Navier-Stokes equations, called *double averaging* (DA), has emerged as a useful technique for quantifying the turbulent flow over the rough boundaries commonly found in rivers. DA has been used to obtain depth-averaged flow quantities, such as the Reynolds Stress (Nikora et al., 2007), and profiles that are independent of heterogeneities caused by flow over the rough and irregular bed. This methodology can be applied to a wide range of river geometries (Nikora et al., 2013). DA has allowed the identification of the *hydrodynamic transition region* in the bed, defined as the location where strong dissipation of momentum by drag forces around sediment grains decreases porewater velocities, turbulent stresses, and pressure fluctuations to laminar flow conditions (Breugem et al., 2006; Manes et al., 2009; Roche et al., 2018; Voermans et al., 2017, 2018; Vollmer et al., 2002). Although other powerful methods have been developed for the identification of structures in flows, such as proper orthogonal decomposition (POD; Beaumard et al., 2019; Berkooz et al., 1993; Meyer et al., 2007), DA has an advantage in that an averaging volume can be explicitly specified, allowing structures above a particular length scale to be highlighted.

Models for hyporheic exchange often solve the Reynolds averaged Navier-Stokes (RANS) equations to assess the overlying flow and the pressure distribution at the sediment-water interface (Bardini et al., 2012; Cardenas, 2008; Kaufman et al., 2017; Zheng et al., 2019). However, the complex and small-scale turbulent interactions in the transition region cannot be accurately resolved by RANS models, so attempts to solve for coupled freestream-porewater flows have concentrated on more computationally taxing but physically accurate techniques. Direct numerical simulation (DNS) has been used (Kuwata & Suga, 2017), but is very computationally expensive and can only be used with low Reynolds number and simple geometries. Large eddy simulations (LES) have been shown to capture the relevant physics (Fang et al., 2018; Lian et al., 2019; Stoesser et al., 2007), and can be more readily upscaled as they are not as computationally expensive as DNS, provided that the subgrid scale is still within the inertial regime. Recent LES simulations have been used not only to capture the coupled fluid-porewater flow, but also to compute lift and drag forces on individual sediment grains, which are important for determining mechanisms of sediment entrainment (Leonardi et al., 2018; Schmeeckle, 2014).
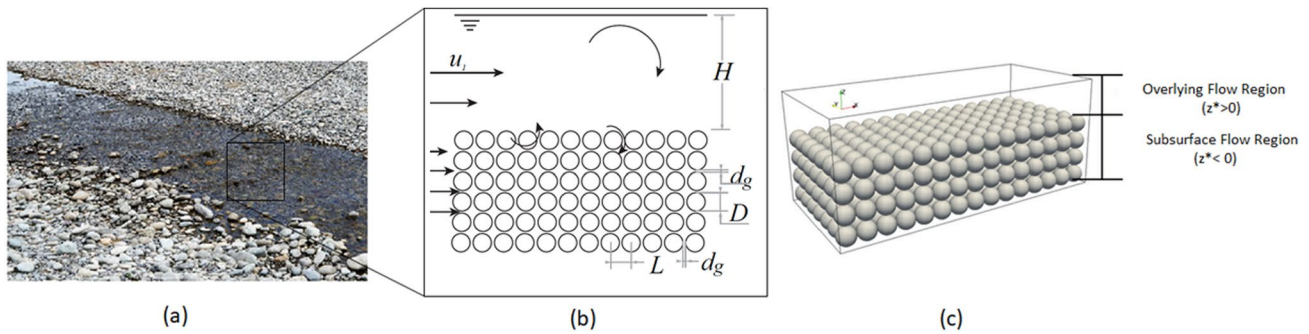
Figure 1. (a) Gravel streambed where turbulent hyporheic exchange has been shown to be important to both flow and biogeochemistry. Image reproduced from Padhi et al. (2019). (b) Schematic of flow structure in water column and porewater. Curved arrows show examples of coherent turbulent structures. For simulations, we consider a flow of depth H over and through a bed of spheres of diameter D with a gap d_g between adjacent spheres. Sphere centers are spaced $L = d_g + D$ apart. The direction of streamwise velocity is u_1 with a minimum shown under the first sphere layer. (c) Three-dimensional bed geometry for large eddy simulations. The mean flow is in the (x) direction and the bed surface is located at $z^* = 0$, where z^* is defined as $z^* = z/L$.

In this study, we use LES to evaluate turbulent flow over and through a bed of coarse spheres, as a model system for understanding hyporheic flow coupling in a gravel bed stream (Figure 1). To identify and quantify the effects of coherent turbulent structures and associated momentum fluxes in the transition region, we apply the double averaging method to LES (DA-LES) over the entire fluid domain, including hyporheic porewater flow in the sediment bed. We then compare our results with prior experimental observations and identify the role of coherent structures in controlling momentum exchange between the overlying flow and porewater. Our analysis advances understanding of turbulence generation at rough, porous interfaces by identifying the types of coherent structures created and the resulting turbulent momentum fluxes into the bed, as well as the drag forces responsible for dissipating momentum in the bed. We use this information to determine the extent of the transition region, which corresponds to the region of the hyporheic zone where turbulence is a significant transport process.

2. Problem and Theory

2.1. Governing Equations

We consider an incompressible fluid flow over and through a three-dimensional bed composed of spheres as shown in Figure 1c. The LES continuity and momentum equations are:

$$\frac{\partial u_i}{\partial x_i} = 0 \tag{1}$$

$$\rho \frac{\partial u_i}{\partial t} + \rho \frac{\partial (u_i u_j)}{\partial x_j} = -\frac{\partial p}{\partial x_i} + \frac{\partial \tau_{ij}}{\partial x_j} - \frac{\partial \tau_{ij}^{SGS}}{\partial x_j} + b_i \tag{2}$$

where u_i is the space-filtered velocity, p is the pressure, ρ is the fluid density, b_i is the body force used to drive the flow, and τ_{ij} and τ_{ij}^{SGS} denote the deviatoric part of the resolved shear viscous stress and unresolved subgrid scale shear stress, respectively. The Einstein summation convention is employed where repeated indices appear. The fluid is assumed Newtonian with a resolved shear stress given by $\tau_{ij} = 2\mu S_{ij}$, where μ is the molecular viscosity and S_{ij} is the resolved rate of deformation, defined as $S_{ij} = \frac{1}{2}(\partial u_i/\partial x_j + \partial u_j/\partial x_i)$.

The wall-adapting local eddy-viscosity (WALE) closure model proposed by Nicoud and Ducros (1999) is applied for the subgrid scale stress, $\tau_{ij}^{SGS} = -2\mu_t S_{ij}$, where μ_t is the eddy viscosity given by:

$$\mu_t = \rho (C_w \Delta)^2 \frac{\left(S_{ij}^d S_{ij}^d\right)^{3/2}}{\left(S_{ij} S_{ij}\right)^{5/2} + \left(S_{ij}^d S_{ij}^d\right)^{5/4}} \tag{3}$$

where the constant C_w is set to 0.325, Δ is the spatial filter. As an unstructured, sphere-surface conforming mesh is used in this study, the spatial filter is tied with the discretization, namely, $\Delta = V^{1/3}$ with V being the volume of the local control volume cell. S_{ij}^d is calculated as

$$S_{ij}^d = \frac{1}{2}\left[\frac{\partial u_i}{\partial x_k}\frac{\partial u_k}{\partial x_j} + \frac{\partial u_j}{\partial x_k}\frac{\partial u_k}{\partial x_i}\right] \tag{4}$$

Unlike some closure schemes (such as the Smagorinsky model), the WALE model is designed so that $\mu_t = 0$ at the wall (Nicoud & Ducros, 1999), which allows the determination of the correct properties (e.g., shear stress and drag forces) when integrating through the viscous sublayer.

2.2. Averaging Techniques for Post-Processing Analysis

We use two decomposition methodologies to transform local instantaneous variables into forms that allow easier interpretation of the governing processes. The first method is the traditional Reynolds decomposition methodology in time, which results in the Reynolds-averaged LES (RA-LES) equations. The other is a double-decomposition technique that is applied to assess larger-scale flow structure and flow-bed interactions integrated over both space and time. In the double-decomposition technique, the time-averaged variables from RA-LES are further decomposed into spatial mean variables and their local spatial fluctuations, leading to the double averaged LES (DA-LES) equations, which differ from the double averaged Navier-Stokes equations (DA-NS) proposed in Nikora et al. (2007, 2001), in that DA-LES includes the subgrid-scale stress as separate terms. This improves calculation of the form and viscous drag forces in the bed, which are critical for the analysis of interactions between overlying flow and porewater flow.

2.2.1. Double Averaged LES Equations

While the double averaging methodology has previously been applied to the Navier-Stokes Equation (Nikora et al., 2001, 2007), here we derive double averaged equations for LES (DA-LES) by applying the superficial spatial averaging equation to the RA-LES equations. A full derivation of the DA-LES equations can be found in Appendix A. The resulting continuity and momentum equations are:

$$\frac{\partial \langle \bar{u}_i \rangle_s}{\partial x_i} = 0 \tag{5}$$

and

$$\rho\frac{\partial \langle \bar{u}_i \rangle_s}{\partial t} + \rho\frac{\partial \langle \overline{u_i u_j} \rangle_s}{\partial x_j} = -\frac{\partial \langle \bar{p} \rangle_s}{\partial x_i} + \frac{\partial \langle \overline{\tau_{ij}} \rangle_s}{\partial x_j} - \frac{\partial \langle \overline{\tau_{ij}^{SGS}} \rangle_s}{\partial x_j} + \frac{\partial \langle \tau_{ij}^R \rangle_s}{\partial x_j} - f_i^{p,s} + f_i^{v,s} + \langle \bar{b}_i \rangle_s \tag{6}$$

where $f_i^{p,s}$ represents the form drag force per unit volume:

$$f_i^{p,s} = -\frac{1}{V_o}\int_{S_{int}} \bar{p} n_i \mathrm{d}A \tag{7}$$

and $f_i^{v,s}$ denotes the viscous drag force per unit volume:

$$f_i^{v,s} = \frac{1}{V_o}\int_{S_{int}} \overline{2\mu S_{ij}} n_j \mathrm{d}A \tag{8}$$

The overbar denotes time averaging, $\langle \cdot \rangle$ denotes spatial averaging, V_o stands for the overall averaging volume, $\tau_{ij}^R = -\rho\overline{u_i' u_j'}$ is the Reynolds stress (where fluctuations are calculated around the LES resolved velocity), and A is the contact area between the fluid and the solid inside V_o, and n_i is the unit normal at A that points from the solid into the fluid. The body force $\bar{b}_i$ is taken as a constant. The WALE model forces $\mu_t = 0$ at solid surfaces, so only the molecular viscosity contributes to the viscous drag.

In addition to the total volume definition, the roughness geometry indicator (ϕ_s) can be applied to write the form drag and viscous drag forces as intrinsic spatial averages.

$$f_i^p = \frac{f_i^{p,s}}{\phi_s} \tag{9}$$

$$f_i^v = \frac{f_i^{v,s}}{\phi_s} \tag{10}$$

where $\phi_s = V_f/V_o$, and V_f is the space occupied by fluid in V_o.

If intrinsic averaging is applied (see Appendix A), alternative formulations of the form and viscous drag forces are:

$$f_i^p = \left\langle \frac{\partial \bar{p}}{\partial x_i} \right\rangle - \frac{1}{\phi_s} \frac{\partial \phi_s \langle \overline{p} \rangle}{\partial x_i} \tag{11}$$

and

$$f_i^v = -\left\langle \frac{\partial (\overline{2\mu S_{ij}})}{\partial x_j} \right\rangle + \frac{1}{\phi_s} \frac{\partial \phi_s \langle \overline{2\mu S_{ij}} \rangle}{\partial x_j} \tag{12}$$

which provide a convenient method for computing the form drag force and viscous drag force from the same averaging volumes used to compute the rest of the terms in Equation 6. To allow for a verification of the drag values in Equations 11 and 12, the drag can also be directly calculated via a direct surface integration on each layer of spheres using Equations 7 and 8.

2.2.2. Simplification of the Double Averaged LES Momentum Equation

For a common flow configuration, turbulent flow over and through a semi-infinite packed granular bed as shown in Figure 1, we assume that the double averaged terms in Equation 6 are functions of z (i.e., x_3) only. For this case, the derivatives of space-averaged quantities are zero in the x and y directions. For steady mean flow, the temporal derivative is also zero. With these assumptions Equation 6 may be simplified as:

$$\rho \frac{d\langle \bar{u}_i \bar{u}_3 \rangle_s}{dx_3} = -\frac{d\langle \overline{p} \rangle_s}{dx_3}\delta_{i3} + \frac{d\langle \overline{\tau_{i3}} \rangle_s}{dx_3} - \frac{d\langle \overline{\tau_{i3}^{SGS}} \rangle_s}{dx_3} + \frac{d\langle \tau_{i3}^R \rangle_s}{dx_3} - f_i^{p,s} + f_i^{v,s} + \langle \overline{b_i} \rangle_s \tag{13}$$

where δ_{i3} is the Kronecker delta function.

Using an xyz coordinate system with (u, v, w) respectively the (x, y, z)-direction velocities, a uniform body force is applied in the x-direction. By periodicity, the x-direction pressure gradient is zero if the averaging volume encompasses the unit cell in the streamwise direction. In this case, Equation 13 may be further simplified by setting $i = 1$:

$$\rho \frac{d\langle \bar{u}\bar{w} \rangle_s}{dz} = \frac{d\langle \overline{\tau_{13}} \rangle_s}{dz} - \frac{d\langle \overline{\tau_{13}^{SGS}} \rangle_s}{dz} + \frac{d\langle \tau_{13}^R \rangle_s}{dz} - f_1^{p,s} + f_1^{v,s} + \langle \overline{b_1} \rangle_s \tag{14}$$

Taking a similar approach but applying the intrinsic averaging equations yields the intrinsic version of the DA-LES momentum equation, which is applied to the LES-computed flow field to evaluate the momentum balances shown in this study.

$$0 = \underbrace{-\frac{\rho}{\phi_s} \frac{d\phi_s \langle \overline{uw} \rangle}{dz}}_{\text{Resolved momentum flux}} + \underbrace{\frac{1}{\phi_s} \frac{d\phi_s \langle 2\mu \overline{S_{13}} \rangle}{dz}}_{\text{Resolved viscous stress}} + \underbrace{\frac{1}{\phi_s} \frac{d\phi_s \langle \overline{2\mu_t S_{13}} \rangle}{dz}}_{\text{Subgrid stress}} +$$

$$\underbrace{f_1^v}_{\text{Viscous drag}} \underbrace{-f_1^p}_{\text{Form drag}} \underbrace{-\frac{\rho}{\phi_s} \frac{d\phi_s \langle \overline{u'w'} \rangle}{dz}}_{\text{Reynolds stress}} + \underbrace{\langle \overline{b_1} \rangle}_{\text{Body force}} \tag{15}$$

Table 1
Permeability Reynolds Number, Bulk Reynolds Number, Bulk Velocity, Sphere Diameter, and Shear Velocity for the DA-LES Simulation Results

	Re_K	Re_B	$U_b(m/s)$	$D(mm)$	$u_*(m/s)$
Simulation	24.2	6,260	0.078	38	0.0094
Experiment	31.2	5,588	0.254	12	0.0215

Note. These dimensionless numbers are similar to the experiments of Manes et al. (2009).

3. Numerical Methods

3.1. Numerical Model

LES is performed on turbulent flow over and through the domain shown in Figure 1c, which simulates an idealized section of a coarse gravel bed stream. The fluid is water with a viscosity of $\mu = 1.002 \times 10^{-3} \frac{kg}{m \cdot s}$ and a density of $\rho = 1 \times 10^3 \frac{kg}{m^3}$. A body force $b_x = 1.1 \frac{kg}{m^2 s^2}$ applied in the streamwise direction drives the flow, which can be characterized by the bulk Reynolds number ($Re_b = U_b \rho H / \mu$) and bed permeability Reynolds number ($Re_K = \sqrt{K} \rho u_* / \mu$). For Re_b, the bulk velocity U_b must be determined using simulation results. For Re_K, K is the bed permeability and is determined for a given sphere diameter via the Carman-Kozeny model (O'Connor & Harvey, 2008; Voermans et al., 2017). The shear velocity, $u_* = \sqrt{\tau_w/\rho} = 9.4 \times 10^{-3}$ m/s is calculated from the wall shear stress τ_w, which is determined from the body force as if the surface of the bed were a planar wall (namely, $\tau_w = b_x H$). Because of the cubically packed nature of the bed, the permeability will be relatively large compared to most natural streams but is close to existing laboratory experimental values (Table 1; Kim et al., 2018; Roche et al., 2018) and a comparable numerical study (Leonardi et al., 2018).

The numerical model and simulation approach are briefly summarized here. As shown in Figure 1b, the *x*-axis is oriented along the mean flow (streamwise) direction parallel to the bed surface, the *y*-axis is the spanwise orthogonal direction, and the *z*- axis is perpendicular to the bed surface pointed upwards into the overlying flow. Periodic boundary conditions are imposed in the streamwise and spanwise directions to model fully developed flow. The top and bottom surfaces are modeled as traction-free surfaces with no penetration. A no-slip condition is imposed at the surface of each sphere, and the simulation is conducted using a control volume finite element method (CVFEM; Schneider & Raw, 1987) implemented in the open-source CFD code Nalu (Domino, 2015).

Given a sphere diameter $D = 38$ mm and a uniform spacing between spheres of $d_g = 2$ mm, the cell length $L = D + d_g = 40$ mm and normalized vertical distance $z^* = \frac{z}{L}$ are used to spatially define the domain, which has dimensions of $15L \times 7L \times 6L$ in *x*, *y*, and *z* directions, respectively. This domain was found to be large enough to allow for the formation of the largest structures, diminishing the impact of spanwise locking on simulation results (Lian et al., 2019). The gap d_g was chosen to be as small as possible without requiring meshing near a singular contact point. This spacing was shown to have no impact on the solution because flow between the spheres remains within the viscous sublayer and is significantly smaller than flow through the open pore spaces (Lian et al., 2019).

An unstructured, sphere-surface conforming mesh consisting of both wedge and tetrahedral element types is applied to the computational domain. The mesh was created using the mesh generation software Trelis Pro 16.0 (Trelis 16, csimsoft). Two main characteristic element sizes are used for different domain regions. In the subsurface flow region, the element size $h_B = 0.16$ mm is used. In the overlying flow region, an element size of $h_F = 0.40$ mm is used for $z^* > 1$, while the unstructured mesh size is graded between h_F and h_B for $0 < z^* < 1$. The sphere surfaces are meshed using a surface conforming mesh. Therefore, a no-slip boundary condition is enforced at sphere boundary nodes and a layer of wedge elements is created by extruding the surface mesh in the wall-normal direction. The first off-surface grid point is located less than two normalized wall units, $l_* = \mu/\rho u_*$ from the boundary. A four-element-thick boundary layer mesh is applied to each sphere: the initial element height is set to $d_g/20$, each layer grows by a factor of 1.2. A mesh refinement study was conducted to ensure that sufficiently small elements were used (Lian et al., 2019).

To ensure a fully developed flow (Reynolds averaged quantities no longer varied), we conducted the simulation involving a three-phase process (Lian et al., 2019). The first phase is run using a large time step $\Delta t = 1$s without an imposed turbulence closure so that a reasonable initial condition can be established for the ensuing phase in a less computational time. Taking the Phase I results as an initial condition, Phase II is run with the WALE closure scheme and a smaller time step of $\Delta t = 0.03$s so that the Courant number never exceeds 1.3. Phase II is run for more than 117 flow-through-times to ensure that changes in the temporal average for both the velocity and pressure are negligible. Using the results of Phase II as an initial condition, Phase III keeps the same simulation parameters and begins collecting running temporal data.
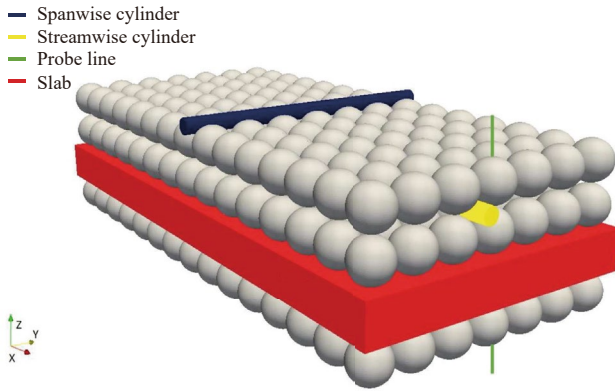
Figure 2. Averaging volumes and lines used. Cylinder averages are used to evaluate flow in pore throats. Slab averages are used to calculate averages over the entire porewater. Probe lines capture instantaneous values in vertical pore throats.

3.2. Data Analysis Post-Processing

Double averaged results are reported using three different types of averaging volumes (as shown in Figure 2). The first averaging volume is a rectangular slab that spans the entire x-y plane and has a thickness $T = L$, ensuring a constant porosity for slabs within the bed itself, independent of z^*. As all the available fluid is sampled, this averaging domain ensures that the various contributing factors to the momentum balance can be evaluated as a function of z^* alone in both the overlying, subsurface and transition regions. Slab averaging volumes were centered at z^* locations separated by increments of $\Delta z^* = \frac{1}{30}$ from $z^* = -3.5$ to $z^* = 1.5$. To investigate the impacts of the averaging volume size, a smaller averaging volume ($T = 0.25L$) was also used.

To compare simulation results with existing experimental data of Manes et al. (2009), cylindrical volumes are used to evaluate mean velocity in bed open pore throats. These volumes allow for comparison with experimental results (that are obtained from open pores). Streamwise cylinders extend the length of the domain in the x-direction and are centered in between two spheres in the y-direction. Spanwise cylinders extend the length of the domain in the y-direction and are centered in between two spheres in the x-direction. Streamwise cylinders of radii 12 mm, are used for all values of z^* while spanwise cylinders of radii 8.333 mm are only used for $-0.17 < z^* < 0$ to emulate the experimental measurement volumes.

4. Results

4.1. Mean Flow

Figure 3 compares the freestream velocity between the simulation and experimental data collected by Manes et al. (2009). Velocities are normalized by the surface bulk velocity U_b, calculated as the double
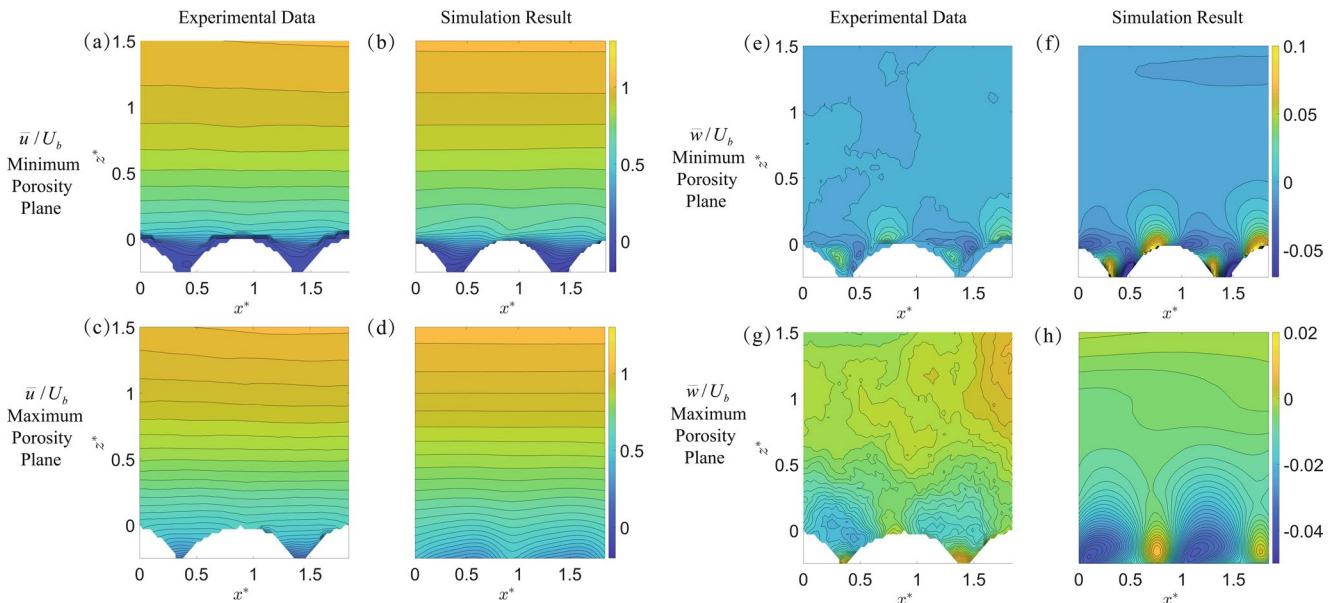
Figure 3. Comparison of the streamwise velocity profiles ($\bar{u}/U_b$ and $\bar{w}/U_b$) between the PIV experimental data from Manes et al. (2009) and the simulation results. The subfigures—(a, c, e, g)—show the experimental results and the subfigures—(b, d, f, h)—show the simulation results. Subfigures (a, b, e, and f) are from a x-z plane of minimum porosity subfigures (c, d, g, and h) are from a x-z plane of maximum porosity. The white semicircles present near bottom of the subfigures are projections of the spheres, showing fluid that is not visible experimentally. As can be seen by comparing (c and d) at $x^* = 1$, there is high velocity fluid below $z^* = 0$ that is obstructed. This high velocity fluid near the interface and associated turbulent fluxes into the porewater will not be measured experimentally.
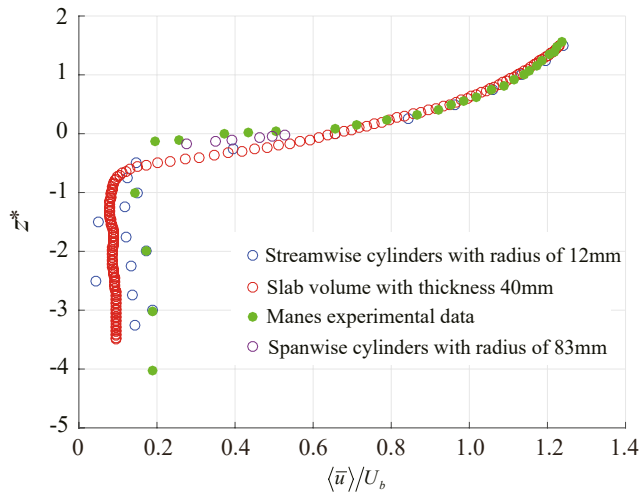
Figure 4. Comparison of double-averaged mean velocity profiles normalized by the bulk velocity (U_b) between the experimental data from Manes et al. (2009) and the simulation results.

averaged streamwise velocity between $-0.5 < z^* < 2$. Bulk flow variables are shown in Figure 3. In the experiment, for $z^* > -0.17$, a particle image velocimetry (PIV) sidewall measurement was used to capture the mean velocity in a plane. This technique leads to flow near the interface being obstructed for planes other than the minimum porosity plane, as shown in Figures 3c and 3g. The simulation adds to the experimental results by showing increased $\bar{u}/U_b$ at $x^* = 1$ and the high and low values of $\bar{w}/U_b$ in the experimentally obstructed region. Particularly for $\bar{w}/U_b$ (Figures 3e–3h), the magnitude of the simulation velocity near the sphere surfaces exceeds the measured velocity. This is attributable to notorious difficulties involved in using PIV near curved walls (Jia et al., 2017; Nguyen et al., 2010), which can lead to both overestimates and underestimates of velocity magnitude (Kähler et al., 2012) Notably, there is close agreement between the simulation and experiment on the location of the local minima and maxima of $\bar{w}/U_b$ on the surfaces of spheres.

Using the averaging volumes detailed in Section 3.2, $\langle \bar{u} \rangle$ as a function of depth is plotted in Figure 4 for both the simulation and experiment (Manes et al., 2009). In the experiment, an ultrasonic velocity profiler (UVP) was used with PIV to collect streamwise velocity data, which were then averaged to produce vertical double averaged streamwise velocity profiles. Both types of experimental data are represented by the green circles in Figure 4. UVP was used to measure the velocity along pore-throats, which was averaged in time and then space. For the UVP data, the spatial averaging volume consists of a truncated cone with a radius that varies with distance from the profiler, beginning at $5/12\ D$ and ending at an indeterminate value. To match the porewater measurement scheme, we averaged LES results using streamwise cylinder volumes with radii of 12 mm (equivalent to $12/19\ D$), as shown by the open blue circles in Figure 4. For $z^* > -0.17$, PIV sidewall measurements were used to capture the mean velocity in a plane. This technique leads to flow near the interface being obstructed for planes other than the minimum porosity plane, as shown in Figures 3c and 3g. To capture the impact of this obstruction, spanwise cylinders with a radius of 8.3 mm (equivalent to $5/12\ D$) were chosen and placed down spanwise pores in the minimum porosity plane, as shown by the open purple circles in Figure 4.

The slab averages show a transition from rapid overlying flow above the spheres to a slower flow in the subsurface region. Velocity magnitude in the overlying flow decreases approaching the bed and continues to decrease steeply through the first layer of spheres. The profile shows a sharp transition near the bottom of the first layer of spheres before a global mean velocity minimum occurs near $z^* = -1.4$. The velocity profile is relatively uniform after the minimum. Slight local minima are located at $z^* = -2.2$ and $z^* = -3.23$ while local maxima are located at $z^* = -1.73$ and $z^* = -2.78$. Minima are 1/4 sphere diameter below open pore throats while maxima are 1/4 sphere diameter above open pore throats. Note that intrinsic averaging was conducted for both the measurements of Manes et al. (2009) and the simulation results, so the differences are indicative of the choice of averaging volume, rather than averaging methodology.

In the overlying flow (i.e., $z^* > 0$), the slab averaging volume simulation results closely match the experimental data. At the interface between the overlying and porewater flows, the experimental mean velocity is smaller than the mean velocity captured by the slab averages. The reason for this difference is that behind the projection of the spheres ($-0.17 < z^* < 0$), high momentum fluid is physically obstructed from view and therefore unmeasured using the experimental methodology as demonstrated in Figure 3c. Averaging along spanwise cylinders reproduces PIV measurements that primarily sample flow in open spanwise pore throats. In the subsurface flow (i.e., $z^* < -0.5$), averaging in streamwise cylinders at pore throats also reproduces the experimental UVP data, which sample subsurface pore throats rather than the full velocity field. Because regions of lower velocity between spheres are obscured in experiments, the experimental mean velocity is larger in the subsurface when compared with the slab averages computed from simulations. The magnitude of the local minima calculated using DA-LES are between 48% and 53% of the values reported by Manes et al., and the subsurface local maxima are less than 65% of the lowest experimental value.

Figure 5. The first row shows comparisons between the simulation and experiment of Manes et al. (2009) for (a) the spatially averaged u' turbulence intensity, (b) the spatially averaged w' turbulence intensity, and (c) the shear Reynolds stress. An averaging volume of $T = 0.25L$ is used for the numerical results and all values are normalized by u^*. In the second row, the vertical profile of spatially averaged Reynolds shear stress $\langle \tau_{13}^R \rangle$ is shown for an averaging volume of $T = L$ (d) and $T = 0.25L$ (e) and the turbulent kinetic energy measured along a vertical probe line in one of the maximum porosity pores is shown in (f). The dashed line shows the sediment-water interface.

4.2. Reynolds Shear Stress and TKE Analysis

Figures 5a–5c show comparisons between the simulation and experiment of Manes et al. (2009) for the spatially averaged turbulence intensities ($\langle \sqrt{\overline{u'u'}} \rangle$ and $\langle \sqrt{\overline{w'w'}} \rangle$) and the Reynolds shear stress ($\langle \tau_{13}^R \rangle$). The spatially averaged turbulence intensities are normalized by the wall shear velocity, which is approximated as $u_* = \sqrt{b_x H/\rho}$ and is discussed in more detail in Lian et al. (2019). As shown in Figures 5a and 5b, the simulation results of turbulence intensities are in good agreement with the experimental data for $z^* > 0$. The experimental values are smaller just below $z^* = 0$, which is probably due to variations in sampling volume (see the obstructions discussed in Section 4.1), noise in the UVP measurement at depth, and underestimation of the w velocity near the spheres due to difficulties with near-wall PIV measurements (Kähler et al., 2012; Jia et al., 2017; Nguyen et al., 2010). Moreover, for the w' turbulence intensity, both the experiment and simulation show a secondary peak near $z^* = -0.4$. For the Reynolds shear stress profiles shown Figure 5c, the simulation profile is in general agreement with the experimental profile, though the experimental profile shows a peak above the first row of spheres while the simulation peak is at $z^* = 0$. It should be noted that the simulation peak location in Figure 5c is consistent with other simulation result of similar geometries (Fang et al., 2018).

The vertical profile of the spatially averaged Reynolds shear stresses $\langle \tau_{13}^R \rangle$ is presented in Figures 5d and 5e. Using an averaging volume with $T = L$ (as shown in Figure 5d), the curve increases linearly with decreasing z when approaching $z^* = 0$ from the overlying flow and then decreases rapidly with penetration into the bed. At $z^* = -1$, $\langle \tau_{13}^R \rangle$ is essentially non-existent. By contrast, an averaging volume with $T = 0.25L$ (as shown in Figure 5e), shows regions of negative shear that appear 1/4 of the way down sphere surfaces while positive peaks appear 3/4 of the way down. Thus, the transition region (here defined as between $z^* = 0$ and

$z^* = -1.0$) emerges as a critical region where turbulence generated at the interface between the overlying and subsurface flows diminishes with depth.

The turbulent kinetic energy (TKE) shows a similar pattern as the Reynolds shear stresses around the interface, as shown in Figure 5f. The spike in the TKE curve just below the top of the first layer of spheres aligns well with the location of the horseshoe vortices and the strongest burst events, showing the increased turbulence generation at this location. Below the interface, TKE is diminished mainly within the transition region. The contribution of each fluctuation ($\overline{u'u'}, \overline{v'v'}, \overline{w'w'}$) to the total TKE along a vertical probe line is plotted in Figure 5f as well. The streamwise component ($\overline{u'u'}$) is dominant throughout. The wall-normal component ($\overline{w'w'}$) is largest in the transition region, but is continuously nonzero to a depth of around $z^* = -2.3$, showing that turbulent transport between the freestream and the bed can occur over multiple sphere layers. The TKE is also nonzero for pore throats deeper in the bed, indicating unsteady flow in these regions.

Both the Reynolds shear stress and TKE are controlled by the coherent structures that can be shown by quadrant analysis and Q-criterion (Hunt et al., 1988) as presented in the following section.

4.3. Visualization of Coherent Turbulent Structures

The quadrant analysis and Q-criterion are used to visualize the coherent structures in the transition region to give physical insight into the double averaged results and the means by which momentum is exchanged between the overlying flow and the porewater.

Using quadrant analysis, the burst events occuring at the sediment-water interface (Stoesser et al., 2007) can be revealed. The burst events include sweep, ejection, inward, and outward burst events, which can be categorized by the velocity fluctuation (u', w'). Sweep events are defined as $u' > 0$ and $w' < 0$ and correspond to influx of higher-momentum fluid from the overlying flow to the subsurface flow. Ejection events are defined as $u' < 0$ and $w' > 0$ and correspond to the expulsion of low-momentum porewater into the overlying flow. In addition to sweeps and ejections, outward ($u' > 0$ and $w' > 0$) and inward ($u' < 0$ and $w' < 0$) events can also be detected. Burst events were characterized by interpolating computed velocities fields at vertical arrays of points (probe lines) shown in Figure 2. The Reynolds averaged velocity was subtracted from the instantaneous measurement at every point and at every stored timestep along the probe line. Based on the sign of u' and w', each event was classified as either a sweep, ejection, inward or outward event. To keep the plot from becoming too densely populated by burst events while still ensuring that a representative sample of events is displayed, each recorded event was separated by $20\Delta t$. A total of 4,000 events were sampled.

The variation in the intensity of sweep events is presented in Figure 6a. In the overlying flow ($z^* = 1$), the intensity and frequency of each event are almost the same, but this begins to change at the sediment-water interface. At the interface ($z^* = 0$), inward events are the weakest and least frequent, accounting for only 13.8% of all events. By contrast, the magnitude of the average ejection and sweep event is 3.3 and 5.0 times that of the average inward event, respectively, and these two events account for over 72% of all events. Sweep and ejection events also predominate above $z^* = -0.5$. The ejection events appear to reach the largest relative contribution at $z^* = -0.125$ while the sweep events peak at $z^* = -0.375$. At $z^* = -0.5$, inward events surpass ejection events in relative magnitude, though ejection events are still frequent. Sweeps continue to play a dominant role well into the first pore space ($z^* = -1.0$). With depth into the subsurface flow, all events diminish in intensity as turbulence is damped.

An example of the key role that ejection and sweep events play in the transition region can be seen in the contour plots in Figures 6b–6d. A single coherent structure can encompass multiple streamwise spheres. The presence of these events is indicative of hyporheic exchange, as the ejection events serve to remove low-momentum fluid from the transition layer, which is replaced by high momentum fluid via sweeps. This process can be seen in Figures 6c and 6d, as a sweep follows closely upon an ejection. The figure also shows the extent to which both coherent structures span multiple sphere diameters, with events including between three and five spheres in the streamwise direction and encompassing at least two spheres in the vertical direction. Stronger sweep events like this one inject momentum vertically downward a significant distance through open vertical pores because the flow is constrained and contribute to the unsteady flow found deeper in the bed (Figure 5f).
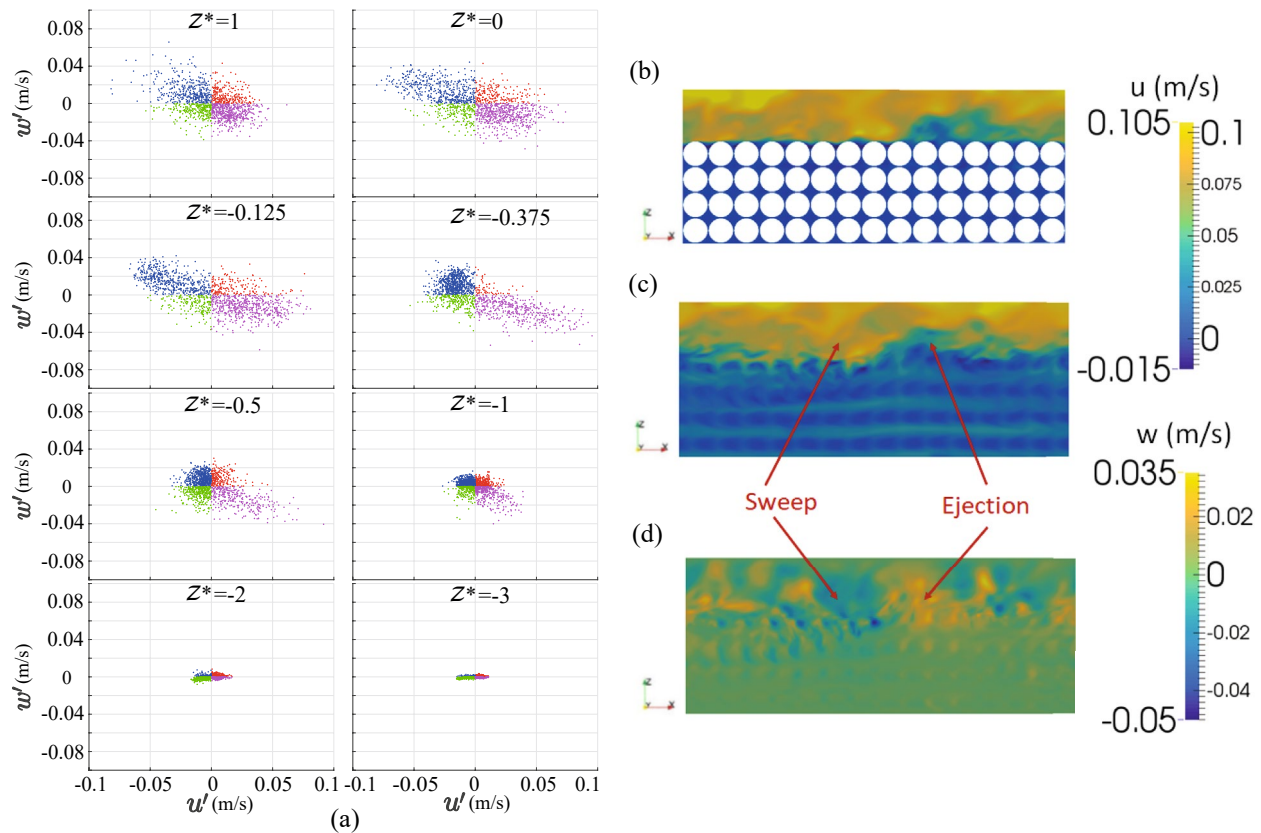
Figure 6. (a) Quadrant mapping of 4,000 burst events, where the relative strength of each event is given by its distance from the origin and different types of events and color show different events. Blue dots denote ejection events, purple are sweeps, green are inward and red are outward. (b–d) Contour plots of instantaneous streamwise velocity in representative xz planes. In (b), the streamwise velocity in a minimum porosity plane ($y = 0.14$ m) is shown, while (c) gives the streamwise velocity in an adjacent maximum porosity plane ($y = 0.12$ m). Interfacial regions of high and low velocity in (b) are visible in (c) showing that the coherent structure has spanwise depth. In (d), the vertical velocity in the maximum porosity plane is shown. The relatively low streamwise and high vertical velocity region indicates the presence of an ejection while the relatively low vertical and high streamwise velocity indicates a sweep event, as indicated. The ejection and sweep events clearly span multiple sphere diameters and inject fluid to a depth of several pores.

Q is defined as the difference between the vorticity $|\Omega_{ij}|$ and the strain rate tensor:

$$Q = 0.5(|\Omega_{ij}|^2 - |S_{ij}|^2) \tag{16}$$

Plots of Q for the flow overlying and in the transition region are shown in Figure 7. The most obvious coherent structures are the horseshoe vortices that form around spheres in the transition region. The hairpin vortices that are often found in flow over impermeable beds (Blois et al., 2012, 2014; Sinha et al., 2017; Stoesser et al., 2007) are not observed here. The horseshoe vortices form on the upstream face of the spheres, between $-0.5 < z^* < 0$, and have arms that extend downstream around the spheres. The vorticity upstream of each sphere is perpendicular to the $x-$direction (see the inserts in Figure 7), and varies in both time and space. The two arms of the horseshoe vortex are counter-rotating within a $y\text{-}z$ plane, with vorticity roughly parallel to the sediment-water interface in the $x-$direction. Depending on the orientation of the arms, vortex tubes either break up as they extend into the first pore or travel along the surface of the bed, up to several sphere lengths, before being swept into the overlying flow. In Figure 7a, the left arm is breaking up as it enters the first pore, while the right arm is being ejected into the overlying flow. Q is largest when the horseshoe vortices are first created between $-0.5 < z^* < 0$.

4.4. Momentum Balance Analysis and Drag Forces

The double averaged results show the importance of the transition region in the production and dissipation of turbulence independent of streamwise and spanwise heterogeneity. Figures 8a and 8b show the vertical
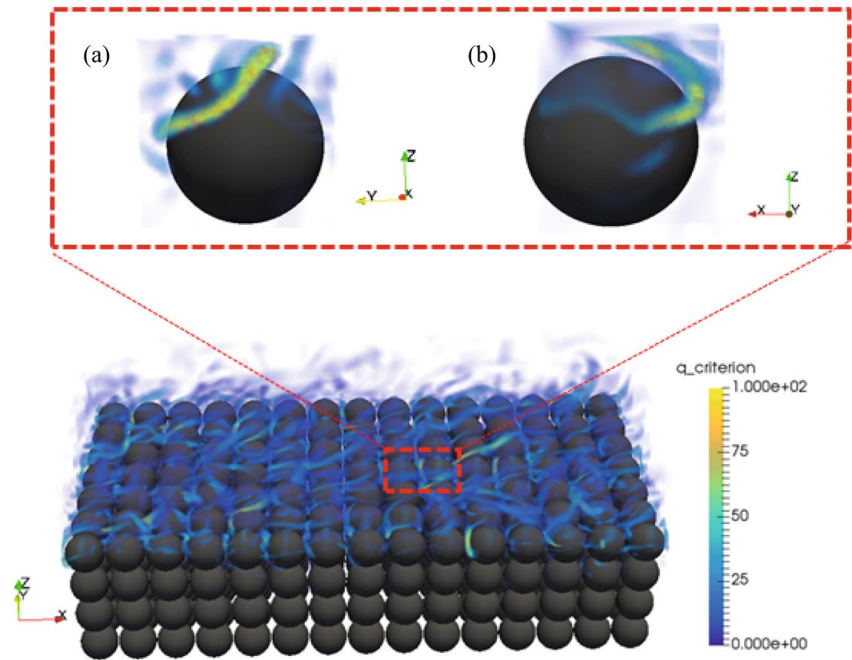
Figure 7. Visualization of coherent structures in the coupled overlying and subsurface flow based on Q-Criteria (scale of 0–100) for all events. Insert shows an example of a horseshoe vortex forming around a sphere centered at $x = 0.38$ m and $y = 0.14$ m in the first layers of spheres at an instant in time. Note that in the insert, (a) shows a y-z plane and (b) shows the x-z plane, with the direction of mean flow is to the left to allow for visualization of the structure.

profile of each term in Equation 15 for slabs of thickness $T = L$ and $T = 0.25L$. For both averaging domains, the sum of all the momentum balance terms is nearly zero, as expected. Averaging volumes of even smaller size ($T < 0.25L$) were also used and gave profiles with the same shape as the $T = 0.25L$ averaging volume. Small non-zero peaks in the sum occur near $z^* = 0.5$ and $z^* = −0.5$ for $T = L$ and $z^* = 0.125$ and $z^* = −0.125$ for $T = 0.25L$, where the porosity of the averaging volume changes substantially near the sediment-water interface. In the overlying flow, the body force is balanced by the Reynolds shear stress. When both averaging volumes transition from the overlying flow to include the interface, increased turbulence generation leads to a rapid increase in the Reynolds shear stress, which is balanced by an increase in both the form and viscous drag forces. The Reynolds shear stress remains an important part of the momentum balance in the first pore space but becomes negligible below $z^* = −1$ for the $T = L$ slabs. For $T = 0.25L$, the Reynolds shear stress oscillates and is positive in planes of low porosity and becomes negative in planes of high porosity. Throughout the homogeneous porous region below $z^* = −1$, the form and viscous drag forces balance the body force and Reynolds shear stress. The form drag force is consistently larger than the viscous drag force in the near-bed and subsurface regions. In the subsurface, the form drag force is over 1.5 times greater than the viscous drag force. These results indicate that form drag force is the major resistance force to flow, as well as the major factor extracting momentum in the subsurface. The value of double averaged subgrid stress contribution to the momentum balance is minimal, showing that our mesh resolution is small enough to capture all but the smallest vortical structures.

The form and viscous drag forces are shown in Figures 8c and 8d. Since a conforming mesh is used, they can be directly compared with the drag forces calculated via Equations 7 and 8. Figures 8c and 8d compare the form and viscous drag profiles with the time-averaged drag and viscous drag force imposed on each sphere at a given bed elevation. The continuous profiles obtained from slab-averaging agree well with the forces integrated over each row of spheres. On the first layer of spheres, the viscous drag force and form drag force are positive, indicating an upwards lift on these spheres. The x and z components of the form drag force are larger contributors to the lift force than the viscous drag force components. For the form drag force, the x component is less than the z component, while for the viscous drag force, the x component is larger than the
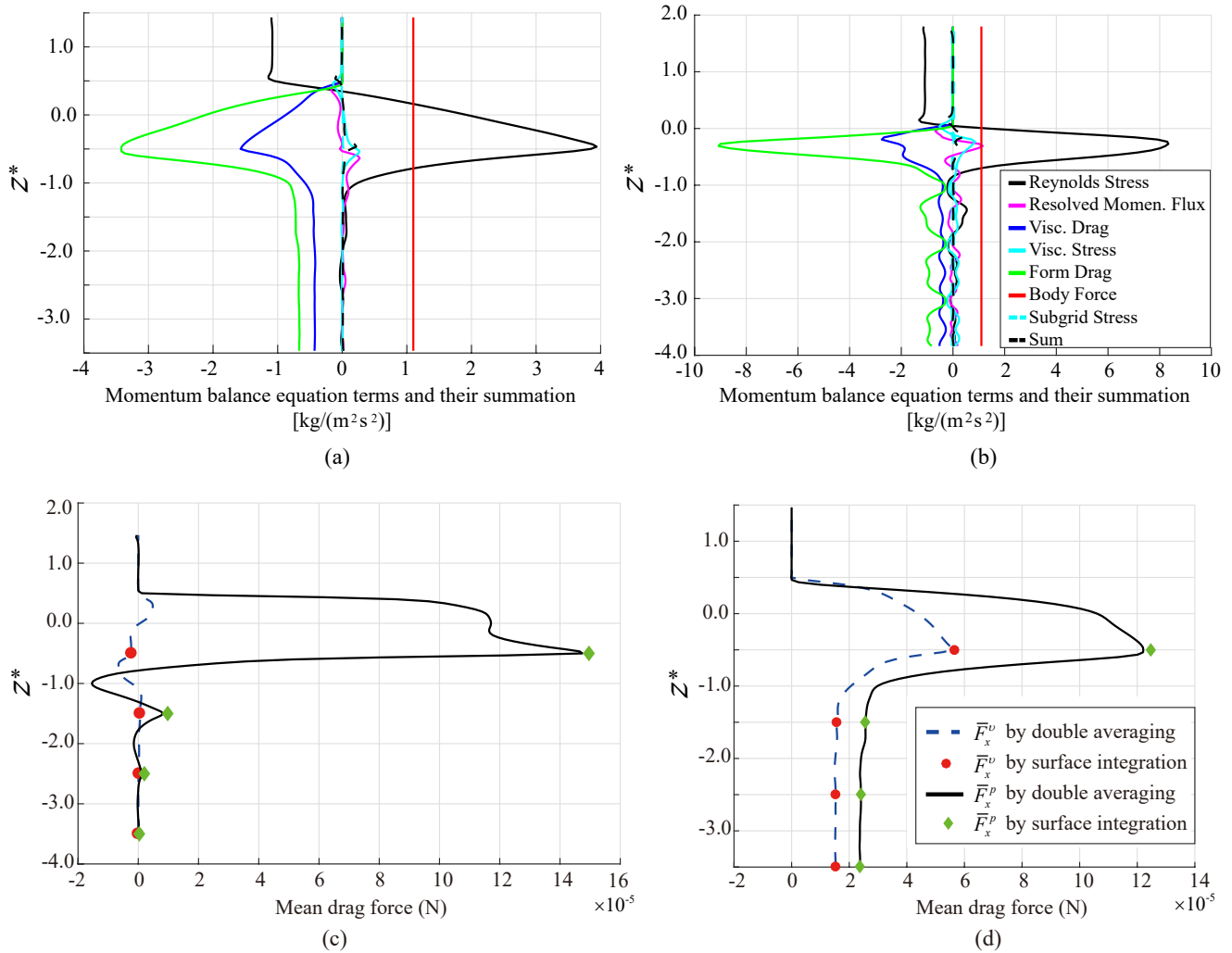
Figure 8. The first row contains the vertical profile of each double averaged momentum term from Equation 15, shown using an averaging volume of $T = L$ (a) and $T = 0.25L$ (b). In the second row, the comparison between the double averaging technique and surface integration technique for the drag forces calculation are shown for the z component (c) and the x component (d). Superscripts p and v denote the form and viscous drag forces.

z component. Deeper in the bed, the x component of form drag force remains the largest contributor, but all drag forces are less than those occurring in the first layer of spheres.

5. Discussion

The results presented in Section 4 advance the understanding of the structure of turbulence at the interface between the overlying flow and the porous bed and the associated coupling between the overlying and porewater flows.

We identify multiple scales of turbulence, including grain-scale vortices and large coherent structures spanning multiple grains, that are generated at the interface and propagate into the porewater. This turbulent transport couples the flow above and within the porous bed. Sweep and ejection events are important contributors to the transfer of momentum into the bed. Ejection events transfer low-momentum fluid to the overlying flow and are strongest just before the low momentum fluid clears the crest of the first sphere ($z^* = 0$). In contrast, sweep events inject high momentum into the pore space, as has been observed experimentally using refractive index matching techniques (Voermans et al., 2018). These events diminish in intensity after the first plane of minimum porosity in the bed ($z^* = -0.5$) as the streamwise velocity is

significantly diminished by interaction with bed sediment grains (as shown in Figure 4). In addition to sweep and ejection events, complex small-scale structures are generated around the first layer of spheres. Horseshoe vortices sporadically form on spheres at the interface. The vortex arms that form on the upstream ends of the sphere are carried downstream by the flow. These vortices primarily propagate upward into the freestream, but some also propagate downward and inject turbulence into underlying pores. Q is largest when the horseshoe vortices are created in the region between $z^* = 0$ and -0.5. The maximum TKE in the bed also occurs in this region. Generation of turbulence at the interface yields large-scale freestream flow structures. In turn, these large structures (Figures 6b–6d) modulate local-scale turbulence by either forcing the arms of the horseshoe vortices into the first pore or ejecting them into the overlying flow (Figure 7). These multi-scale interactions control interfacial fluxes and are important to hyporheic biogeochemistry, as interfacial turbulence is known to control hyporheic nutrient dynamics and transformation rates (Grant, Gomez-Velez, et al., 2018; Manes et al., 2011; Reidenbach et al., 2010; Roche et al., 2018).

The extent of the transition region can also be identified using double averaging. In Figure 8, the maximum Reynolds stresses and drag forces occur at around $z^* = -0.5$, half a sphere diameter below the bed surface for $T = L$, and at $z^* = -0.3$ for $T = 0.25L$. This region is influenced by coherent structures originating from the tops of the first row of spheres, where burst events increase in strength and horseshoe vortices form. In addition, the Reynolds shear stress peaks at $z^* = 0.0$ for both averaging volumes in Figures 5d and 5e, indicating that the transition region begins directly at the interface ($z^* = 0.0$).

While point measurements (Figure 5f) and instantaneous observations (Figures 6b–6d) show that turbulence events can extend from the freestream to at least a depth of $z^* = -2$, DA-LES averaging more clearly identifies the extent of turbulent exchange corresponding to the bottom of the transition region. The Reynolds shear stress (Figures 5d and 5e) rapidly declines with depth below $z^* = 0.0$, becoming small near $z^* = -1.0$ and very close to zero beyond a depth of $z^* = -1.5$. Because of variations in the porosity of the bed below $z^* = -1.0$, smaller averaging volumes show a great deal of variability in the form drag, viscous drag and Reynolds shear stress. It is noteworthy that the larger averaging volume—which gives constant porosity below $z^* = 0.5$—shows negligible variation in drag and Reynolds stress below $z^* = -1.0$. Therefore, the variations in the $T = 0.25L$ case result only from the alignment of spheres in bed, while $T = L$ allows for a better identification of the transition region.

Taken together, these results indicate that the region between $z^* = 0$ and $z^* = -1.0$ is the primary transition region from highly turbulent overlying flow to Darcy flow deeper in the bed. For the given D and Re_K, prior work (Voermans et al., 2018) suggests that the lower bound of the transition region should occur near $z^* = -0.7$. The close alignment between the bottom of the first row of spheres and the transition region at $z^* = -1.0$ highlights the importance of pore connectivity and bed heterogeneity in determining the extent of the transition region. The connected pores in the cubically packed bed contain enhanced porewater velocity and turbulence, resulting in a deeper transition region. In rivers, both the distribution of gravel orientation and the formation of aligned and layered structures (e.g., armor layers and preferential flow paths) control the depth of the transition region (Packman et al., 2004; Tonina & Buffington, 2009).

The extent of the transition region is important for modeling coupled freestream-porewater flows such as rivers. Because the turbulence induced by the interaction between the freestream and porous bed is strongest in the transition region, semi-coupled models risk oversimplifying the system by simply specifying a boundary condition at $z^* = 0$. Accurate modeling of the full domain requires consideration of turbulence in the transition region. Double averaging techniques, in this case DA-LES, advance understanding of this problem by determining the relative importance of internal fluid forces (viscous drag) and fluid-solid interaction forces (form drag). Figures 8c and 8d show the form and viscous drag forces computed as smooth functions of depth through a volume. We found that the form drag is significantly greater than the viscous drag in the transition region (Figure 8d), but viscous and form drag forces have similar magnitudes in deeper pores. Interaction between the highly turbulent overlying flow and the first row of spheres increases the form drag. We also found that the velocity in the first pore throat (below the first row of spheres in the bed) is less than in deeper pore throats. This behavior has been observed previously in experimental studies (Pokrajac et al., 2007), but experimental measurements have not been able to resolve the mechanism for this apparently anomalous velocity minimum in the first layer of pores. Our simulations show that the velocity minimum results from the injected turbulence making the first pore hydraulically rough, which increases

form drag and reduces mean velocity relative to deeper pores that are less turbulent. This new process understanding also clarifies the role of turbulence in mobilizing particles in the active layer of bed sediment transport (Church & Haschenburger, 2017; Dey & Ali, 2019). Our results support the concept that coherent structures entrain sediments (Hardy et al., 2016) by showing that these turbulent structures increase lift forces on grains in the transition region. Recent numerical studies have investigated the implications of these processes for sediment transport (Leonardi et al., 2018; Maniatis et al., 2020; Yang & Nepf, 2018). DA-LES aids this work by enabling the smooth calculation of spatially and temporally averaged lift and drag forces independent of surface integration over a single bed sphere.

DA-LES provides more information than can be obtained via typical experimental observations because, while LES completely resolves the entire porewater flow field, many experimental measurements are limited by physical access and are therefore constrained toward the more open parts of the flow. As a result, available observations only sample the overlying unobstructed flow and open pores within the bed. Because these open pore throats contain the highest velocity fluid in the subsurface, they do not capture the mean subsurface velocity or transport in the bed. Double averaging, in this case by DA-LES, significantly improves understanding of the velocity profile by averaging over regions that are not accessible to physical measurement. We find that the average subsurface velocity is approximately half what would be expected solely on sampling from open pore throats, as shown in Figure 4. Although it has not been used in this work, the combination of POD with DA-LES applied to simulation results might further clarify flow structures at the hyporheic interface.

In addition to clarifying the flow structure and mechanisms of turbulent momentum transport, our results directly apply to solute transport across the bed surface and within porewater. Our results show very strong turbulent interaction with the top few layers of bed sediment grains, as evidenced by the TKE depth profile in Figure 5f and the presence of sustained coherent structures in Figure 7. All of these turbulent processes accelerate mass transport across the bed surface and into porewater. Turbulent hyporheic exchange is known to influence biogeochemical processes at the scale of the entire stream by controlling hyporheic fluxes and residence times in the transition region, where microbial activity and chemical reactivity are both very high (Grant, Gomez-Velez, et al., 2018; Knapp et al., 2017; Li et al., 2017; Roche et al., 2019). While DNS remains useful for understanding small-scale processes in rivers, LES is better suited to the investigation of highly turbulent flow on reach-scale mass transport as is less computationally expensive. Moreover, the spatial averaging inherent in DA-LES means that this method can be used to identify the extent of the transition region for a wide range of spatial heterogeneity in the bed, potentially via the implementation of an immersed boundary framework (Mittal & Iaccarino, 2005), making it useful for investigating links between bed structure and flow structure in gravel-bed rivers. Further, the computational efficiency of LES and the ability to implement a consistent DA-LES approach across a wide range of scales provides a means to represent the complex, coupled flow and transport dynamics between rivers and hyporheic porewater. This framework can be used to meet the well-established need to relate turbulent porewater transport, flow structures generated by complex river channel geometries, and large-scale physical, morphological, and biogeochemical patterns in rivers (Boano et al., 2014; Grant, Gomez-Velez, et al., 2018; Ward & Packman, 2019). The results presented here provide essential information on turbulent porewater flow and forces on sediment grains in the hyporheic transition region and can be upscaled using either multiscale DA-LES or to improve the parameterization of turbulent transport in existing hyporheic exchange models (e.g., Grant, Gomez-Velez, et al., 2018; Li et al., 2017; Roche et al., 2019).

6. Conclusions and Implications

Our simulations showed that strong coupling between the overlying turbulent flow and subsurface flow leads to a distinct transition region between these flow regimes. We found that the transition region ($-1.0 < z^* < 0$) is the primary location for the formation of coherent turbulent structures and thus the generation of TKE. For $-0.5 < z^* < 0$, strong sweep and ejection events cause horseshoe vortices to form on the surfaces of the bed grains, and these events control the transfer of momentum from the overlying flow to the porewater. At the bottom of the first layer of spheres ($z^* = -1.0$), the mean velocity, form drag, and viscous drag forces become constant and the layer-averaged Reynolds shear stress becomes very small. Our results clearly demonstrate that form drag is the major factor extracting momentum from the flow in the

subsurface and transition region, supporting previous assessments based on experimental observations. However, simulation results agreed well with experimental results from the literature only when the averaging volume was restricted to open pore throats accessible to PIV and UVP measurements. The DA-LES velocity profile shows that porewater mean velocities are almost half what they would be based on simply sampling the pore throats, and that the minimum mean porewater velocity occurs at a depth of $z^* = -1.4$ instead of in the first pore throat ($z^* = -1.0$) suggested by experiments. The velocity minimum occurs at $z^* = -1.4$ due to large-scale turbulent structures that preferentially propagate into open pore throats, yielding stagnation points above the midline of the second row of spheres. These dynamics are better captured by experimental methods that enable observation of the entire porewater, such as refractive index matching (Kim et al., 2018; Voermans et al., 2017).

Double averaging supports proper determination of the momentum balance and profiles of key flow quantities with full consideration of streamwise and spanwise heterogeneities in the bed surface morphology and underlying pore structure. This makes DA-LES a useful tool for relating hydrodynamic processes to hyporheic exchange and mass transport in rivers. DA-LES provides a framework for directly parameterizing the effects of interfacial and porewater flows in upscaled transport models. Pairing DA-LES with Lagrangian particle tracking techniques may provide a useful pathway to achieving this long-term objective of hyporheic research. Particle tracking has recently been used to determine diffusion coefficients and residence times in surface waters, groundwaters, and across the stream-subsurface interface (Li et al., 2017, 2021; Sherman et al., 2019; Sund et al., 2015). With sufficient computing power and system information, profiles of mean velocity, Reynolds stress, and turbulent diffusion generated via LES can be double averaged and then used to directly calculate effective transport properties for both the water column and subsurface over the range of scales commonly encountered in rivers (Grant, Gomez-Velez, et al., 2018; Harvey et al., 2013). This approach represents an extension of the well-established eddy diffusivity approximation to correlate turbulent transport with mean flow quantities. While classical methods are only applicable in the water column, LES resolves turbulent flow in the entire fluid continuum, and double averaging can be used to obtain meaningful space-averaged and time-averaged transport properties across the sediment-water interface. While considerable effort will be required to apply these methods in natural systems, the long-term potential of this approach is to obtain upscaled transport predictions in rivers that are directly informed by mechanistic understanding of the channel morphology, bed properties, and turbulent flow field.

Appendix A: Derivation of the DA-LES Equations

Appendix A1: Reynolds Decomposition Methodology

Based on well-known double averaging theory (Nikora et al., 2001; Whitaker, 1985), for a LES resolved flow variable, $\theta(\boldsymbol{X}, t)$, the Reynolds decomposition is defined as

$$\theta = \bar{\theta} + \theta' \tag{A1}$$

where an overbar denotes time averaging, and the prime represents the deviation from the mean. Using the Reynolds decomposition methodology on Equations 1 and 2 leads to the RA-LES equations.

$$\frac{\partial \bar{u}_i}{\partial x_i} = 0 \tag{A2}$$

and

$$\rho \frac{\partial \bar{u}_i}{\partial t} + \rho \frac{\partial (\bar{u}_i \bar{u}_j)}{\partial x_j} = -\frac{\partial \bar{p}}{\partial x_i} + \frac{\partial \overline{\tau_{ij}}}{\partial x_j} - \frac{\partial \overline{\tau_{ij}^{SGS}}}{\partial x_j} + \frac{\partial \tau_{ij}^R}{\partial x_j} + \bar{b}_i \tag{A3}$$

where $\tau_{ij}^R = -\rho \overline{u_i' u_j'}$ is the Reynolds stress (where fluctuations are calculated around the LES resolved velocity). The body force $\bar{b}_i$ is taken as a constant.

Appendix A2: Double Average Methodology

The double averaging of a flow variable involves taking both a temporal and spatial average. The spatial averaging is typically done over a defined averaging volume, as will be done here. If V_f is the space occupied by fluid in the overall averaging volume V_o, for a general flow variable θ the intrinsic spatial average and superficial spatial average are:

$$\langle\theta\rangle(\boldsymbol{X},t) = \frac{1}{V_f}\int_{V_f}\theta\,\mathrm{d}V, \quad \langle\theta\rangle_s(\boldsymbol{X},t) = \frac{1}{V_o}\int_{V_f}\theta\,\mathrm{d}V \tag{A4}$$

where $\langle\cdot\rangle$ denotes spatial averaging. The subscript s distinguishes the superficial and intrinsic averages, which are related through the porosity ϕ_s, as follows:

$$\langle\theta\rangle_s = \phi_s\langle\theta\rangle \tag{A5}$$

where $\phi_s = V_f/V_o$. Above the top row of spheres, $\phi_s = 1$ while $\phi_s \leq 1$ in the bed.

There are two options for ordering the decomposition of a temporally and spatially varying quantity—spatial then temporal or temporal then spatial averaging. As it has been shown that both approaches lead to the same double average momentum equations (Pedras & de Lemos, 2001; Pokrajac, 2007), here we use the time-space ordering as it is consistent with traditional turbulence analysis and gives us understandable physical properties based on the temporal fluctuations (the Reynolds stress) (Nikora et al., 2007).

Using this averaging order, the spatial average of a time-averaged general flow variable θ can be decomposed as

$$\bar{\theta} = \langle\bar{\theta}\rangle + {\sim}\theta \tag{A6}$$

where $\tilde{}$ indicates the spatial fluctuation around the double averaged variable.

Relationships between the double average operator with time and space differentiations are defined by the transport theorem and spatial-averaging theorem, as introduced in Whitaker (1985, 1986). Assuming that solids in the domain are immobile and impermeable and the fluid velocity is zero on solid surfaces, the intrinsic temporal-averaging and spatial-averaging theorems (Slattery, 1999; Whitaker, 1999) are as follows.

$$\left\langle\frac{\partial\bar{\theta}}{\partial t}\right\rangle = \frac{1}{\phi_s}\frac{\partial(\phi_s\langle\bar{\theta}\rangle)}{\partial t} \tag{A7}$$

$$\left\langle\frac{\partial\bar{\theta}}{\partial x_i}\right\rangle = \frac{1}{\phi_s}\frac{\partial(\phi_s\langle\bar{\theta}\rangle)}{\partial x_i} - \frac{1}{V_f}\int_{S_{int}}\bar{\theta}n_i\,\mathrm{d}A \tag{A8}$$

where A is the contact area between the fluid and the solid inside V_o, and n_i is the unit normal at A that points from the solid into the fluid.

Spatial averaging is applied to each term in the RA-LES continuity (Equation A2) and momentum (Equation A3) equations to obtain the DA-LES equations.

Appendix A3: Derivation Using Superficial Averaging

First, the spatial-averaging theorem (Equation A8) is applied to the continuity equation

$$0 = \left\langle\frac{\partial\bar{u}_i}{\partial x_i}\right\rangle_s = \frac{\partial\phi_s\langle\bar{u}_i\rangle}{\partial x_i} - \frac{1}{V_o}\int_{S_{int}}\bar{u}_i n_i\,\mathrm{d}A$$

Because we define a no-slip condition on the surface of each sphere, the surface integral is zero and the above simplifies to the following superficial average which is Equation 5

$$\frac{\partial\langle\bar{u}_i\rangle_s}{\partial x_i} = 0$$

Equation A3 can also be spatially averaged

$$\left\langle \rho \frac{\partial \overline{u}_i}{\partial t} \right\rangle_s + \left\langle \rho \frac{\partial \overline{u}_i \overline{u}_j}{\partial x_j} \right\rangle_s = \left\langle -\frac{\partial \overline{p}}{\partial x_i} \right\rangle_s + \left\langle \frac{\partial \overline{\tau}_{ij}}{\partial x_j} \right\rangle_s + \left\langle -\frac{\partial \overline{\tau_{ij}^{SGS}}}{\partial x_j} \right\rangle_s + \left\langle \frac{\partial \tau_{ij}^{R}}{\partial x_j} \right\rangle_s + \langle \overline{b}_i \rangle_s \tag{A9}$$

Each term of Equation A9 can be spatially averaged. First, the transport theorem is used on the time derivative on the left-hand side of the RA-LES momentum equation (Equation A3)

$$\left\langle \rho \frac{\partial \overline{u}_i}{\partial t} \right\rangle_s = \rho \frac{\partial \langle \overline{u}_i \rangle_s}{\partial t} \tag{A10}$$

The second term on the left-hand side of Equation A3 is spatially averaged using the spatial-averaging theorem and the no-slip condition on sphere surfaces

$$\left\langle \rho \frac{\partial \overline{u}_i \overline{u}_j}{\partial x_j} \right\rangle_s = \rho \left\langle \frac{\partial \overline{u}_i \overline{u}_j}{\partial x_j} \right\rangle_s = \rho \frac{\partial \langle \overline{u}_i \overline{u}_j \rangle_s}{\partial x_j} - \frac{\rho}{V_o} \int_{S_{int}} \overline{u}_i \overline{u}_j n_j \mathrm{d}A$$

$$\left\langle \rho \frac{\partial \overline{u}_i \overline{u}_j}{\partial x_j} \right\rangle_s = \rho \frac{\partial \langle \overline{u}_i \overline{u}_j \rangle_s}{\partial x_j} \tag{A11}$$

For the right-hand side, the spatial-averaging theorem is used to average the pressure derivative term

$$\left\langle -\frac{\partial \overline{p}}{\partial x_i} \right\rangle_s = -\frac{\partial \langle \overline{p} \rangle_s}{\partial x_i} + \frac{1}{V_o} \int_{S_{int}} \overline{p} n_i \mathrm{d}A \tag{A12}$$

The resolved and unresolved shear stress terms can be averaged and written in terms of the resolved rate of deformation as follows:

$$\left\langle \frac{\partial \overline{\tau}_{ij}}{\partial x_j} \right\rangle_s = \left\langle \frac{\partial \overline{2\mu S_{ij}}}{\partial x_j} \right\rangle_s = \frac{\partial \langle \overline{\tau}_{ij} \rangle_s}{\partial x_j} - \frac{1}{V_o} \int_{S_{int}} \overline{2\mu S_{ij}} n_j \mathrm{d}A \tag{A13}$$

$$\left\langle -\frac{\partial \overline{\tau_{ij}^{SGS}}}{\partial x_j} \right\rangle_s = \left\langle -\frac{\partial \overline{2\mu_t S_{ij}}}{\partial x_j} \right\rangle_s = -\frac{\partial \langle \overline{\tau_{ij}^{SGS}} \rangle_s}{\partial x_j} + \frac{1}{V_o} \int_{S_{int}} \overline{2\mu_t S_{ij}} n_j \mathrm{d}A \tag{A14}$$

The spatial averaging of the Reynolds stress also makes use of the no-slip condition on the sphere surfaces

$$\left\langle \frac{\partial \tau_{ij}^{R}}{\partial x_j} \right\rangle_s = \left\langle \frac{\partial -\overline{\rho u_i' u_j'}}{\partial x_j} \right\rangle_s = \frac{\partial \langle \tau_{ij}^{R} \rangle_s}{\partial x_j} + \frac{1}{V_o} \int_{S_{int}} \overline{\rho u_i' u_j'} n_j \mathrm{d}A$$

$$\left\langle \frac{\partial \tau_{ij}^{R}}{\partial x_j} \right\rangle_s = \frac{\partial \langle \tau_{ij}^{R} \rangle_s}{\partial x_j} \tag{A15}$$

Equations A10–A15 are substituted into Equation A9

$$\rho \frac{\partial \langle \overline{u}_i \rangle_s}{\partial t} + \rho \frac{\partial \langle \overline{u}_i \overline{u}_j \rangle_s}{\partial x_j} =$$

$$-\frac{\partial \langle \overline{p} \rangle_s}{\partial x_i} + \frac{1}{V_o} \int_{S_{int}} \overline{p} n_i \mathrm{d}A + \frac{\partial \langle \overline{\tau}_{ij} \rangle_s}{\partial x_j} - \frac{1}{V_o} \int_{S_{int}} \overline{2\mu S_{ij}} n_j \mathrm{d}A - \frac{\partial \langle \overline{\tau_{ij}^{SGS}} \rangle_s}{\partial x_j} + \frac{1}{V_o} \int_{S_{int}} \overline{2\mu_t S_{ij}} n_j \mathrm{d}A + \frac{\partial \langle \tau_{ij}^{R} \rangle_s}{\partial x_j} + \langle \overline{b}_i \rangle_s$$

which simplifies to Equation 6

$$\rho \frac{\partial \langle \overline{u}_i \rangle_s}{\partial t} + \rho \frac{\partial \langle \overline{u}_i \overline{u}_j \rangle_s}{\partial x_j} = -\frac{\partial \langle \overline{p} \rangle_s}{\partial x_i} + \frac{\partial \langle \overline{\tau}_{ij} \rangle_s}{\partial x_j} + \frac{\partial \langle \overline{\tau_{ij}^{SGS}} \rangle_s}{\partial x_j} + \frac{\partial \langle \tau_{ij}^{R} \rangle_s}{\partial x_j} - f_i^{p,s} + f_i^{v,s} + \langle \overline{b}_i \rangle_s$$

where $f_i^{p,s}$ and $f_i^{v,s}$ are defined in Equations 7 and 8, respectively.

Appendix A4: Derivation Using Intrinsic Averaging

By converting into an intrinsic average using Equation A8, Equation A2 can be given in its intrinsic form as:

$$\frac{\partial \phi_s \langle \bar{u}_i \rangle}{\partial x_i} = 0$$

Equation A3 becomes

$$\left\langle \rho \frac{\partial \bar{u}_i}{\partial t} \right\rangle + \left\langle \rho \frac{\partial \bar{u}_i \bar{u}_j}{\partial x_j} \right\rangle = \left\langle -\frac{\partial \bar{p}}{\partial x_i} \right\rangle + \left\langle \frac{\partial \overline{\tau_{ij}}}{\partial x_j} \right\rangle + \left\langle -\frac{\partial \overline{\tau_{ij}^{SGS}}}{\partial x_j} \right\rangle + \left\langle \frac{\partial \tau_{ij}^R}{\partial x_j} \right\rangle + \langle \bar{b}_i \rangle \tag{A16}$$

Each term can be evaluated individually using the following:

$$\left\langle \rho \frac{\partial \bar{u}_i}{\partial t} \right\rangle = \rho \frac{1}{\phi_s} \frac{\partial \phi_s \langle \bar{u}_i \rangle}{\partial t} \tag{A17}$$

$$\left\langle \rho \frac{\partial \bar{u}_i \bar{u}_j}{\partial x_j} \right\rangle = \rho \frac{1}{\phi_s} \frac{\partial \phi_s \langle \bar{u}_i \bar{u}_j \rangle}{\partial x_j} \tag{A18}$$

$$\left\langle -\frac{\partial \bar{p}}{\partial x_i} \right\rangle = -\frac{1}{\phi_s} \frac{\partial \phi_s \langle \bar{p} \rangle}{\partial x_i} + \frac{1}{V_f} \int_{S_{int}} \bar{p} n_i \mathrm{d}A \tag{A19}$$

$$\left\langle \frac{\partial \overline{\tau_{ij}}}{\partial x_j} \right\rangle = \left\langle \frac{\partial \overline{2\mu S_{ij}}}{\partial x_j} \right\rangle = \frac{1}{\phi_s} \frac{\partial \phi_s \langle \overline{\tau_{ij}} \rangle}{\partial x_j} - \frac{1}{V_f} \int_{S_{int}} \overline{2\mu S_{ij}} n_j \mathrm{d}A \tag{A20}$$

$$\left\langle -\frac{\partial \tau_{ij}^{SGS}}{\partial x_j} \right\rangle = \left\langle -\frac{\partial \overline{2\mu_t S_{ij}}}{\partial x_j} \right\rangle = -\frac{1}{\phi_s} \frac{\partial \phi_s \langle \tau_{ij}^{\overline{SGS}} \rangle}{\partial x_j} + \frac{1}{V_f} \int_{S_{int}} 2\bar{\mu_t} S_{ij} n_j \mathrm{d}A \tag{A21}$$

$$\left\langle \frac{\partial \tau_{ij}^R}{\partial x_j} \right\rangle = \frac{1}{\phi_s} \frac{\partial \phi_s \langle \tau_{ij}^R \rangle}{\partial x_j} \tag{A22}$$

Data Availability Statement

Data are publicly available from the Hydroshare repository (https://www.hydroshare.org/resource/5f0cbf2e646e4aafbf148088f1bb4d1a/).

References

Bardini, L., Boano, F., Cardenas, M. B., Revelli, R., & Ridolfi, L. (2012). Nutrient cycling in bedform induced hyporheic zones. *Geochimica et Cosmochimica Acta*, *84*, 47–61. https://doi.org/10.1016/j.gca.2012.01.025

Beaumard, P., Buxton, O. R. H., & Keylock, C. J. (2019). The importance of non-normal contributions to velocity gradient tensor dynamics for spatially developing, inhomogeneous, turbulent flows. *Journal of Turbulence*, *20*(9), 577–598. https://doi.org/10.1080/14685248.2019.1685095

Berkooz, G., Holmes, P., & Lumley, J. L. (1993). The proper orthogonal decomposition in the analysis of turbulent flows. *Annual Review of Fluid Mechanics*, *25*(1), 539–575. https://doi.org/10.1146/annurev.fl.25.010193.002543

Blois, G., Best, J. L., Smith, G. H. S., & Hardy, R. J. (2014). Effect of bed permeability and hyporheic flow on turbulent flow over bed forms. *Geophysical Research Letters*, *41*(18), 6435–6442. https://doi.org/10.1002/2014gl060906

Blois, G., Sambrook Smith, G. H., Best, J. L., Hardy, R. J., & Lead, J. (2012). Quantifying the dynamics of flow within a permeable bed using time-resolved endoscopic particle imaging velocimetry (EPIV). *Experiments in Fluids*, *53*, 51–76. https://doi.org/10.1007/s00348-011-1198-8

Boano, F., Harvey, J. W., Marion, A., Packman, A. I., Revelli, R., Ridolfi, L., & Wörman, A. (2014). Hyporheic flow and transport processes: Mechanisms, models, and biogeochemical implications. *Review of Geophysics*, *52*, 603–679. https://doi.org/10.1002/2012RG000417

Boano, F., Revelli, R., & Ridolfi, L. (2011). Water and solute exchange through flat streambeds induced by large turbulent eddies. *Journal of Hydrology*, *402*, 290–296. https://doi.org/10.1016/j.jhydrol.2011.03.023

Breugem, W. P., Boersma, B. J., & Uittenbogaard, R. E. (2006). The influence of wall permeability on turbulent channel flow. *Journal of Fluid Mechanics*, *562*, 35. https://doi.org/10.1017/s0022112006000887

Cardenas, M. B. (2008). The effect of river bend morphology on flow and timescales of surface water–groundwater exchange across point-bars. *Journal of Hydrology*, *326*(1–2), 134–141. https://doi.org/10.1016/j.jhydrol.2008.08.018

Church, M., & Haschenburger, J. K. (2017). What is the "active layer"? *Water Resources Research*, *53*(1), 5–10. https://doi.org/10.1002/2016wr019675

Dade, W. (2001). Multiple scales in river basin morphology. *American Journal of Science*, *310*(1), 60–73. https://doi.org/10.2475/ajs.301.1.60

Dey, S., & Ali, S. Z. (2019). Bed sediment entrainment by streamflow: State of the science. *Sedimentology*, *66*(5), 1449–1485. https://doi.org/10.1111/sed.12566

Domino, S. (2015). "Sierra Low Mach Module: Nalu Theory Manual 1.0", SAND2015-3107W, Sandia National Laboratories Unclassified Unlimited Release (UUR), 2015, Retrieved from https://github.com/spdomin/NaluDoc

Elliott, A., & Brooks, N. (1997a). Transfer of nonsorbing solutes to a streambed with bed forms: Laboratory experiments. *Water Resources Research*, *33*, 137–151. https://doi.org/10.1029/96WR02783

Elliott, A., & Brooks, N. (1997b). Transfer of nonsorbing solutes to a streambed with bed forms: Theory. *Water Resources Research*, *33*(1), 123–136. https://doi.org/10.1029/96WR02784

Fang, H., He, H. X. G., Dey, S., & Dey, S. (2018). Influence of permeable beds on hydraulically macro-rough flow. *Journal of Fluid Mechanics*, *847*, 552–590. https://doi.org/10.1017/jfm.2018.314

Grant, S. B., Azizian, M., Cook, P., Boano, F., & Rippy, M. (2018a). Factoring stream turbulence into global assessments of nitrogen pollution. *Science*, *359*(6381), 1266–1269. https://doi.org/10.1126/science.aap8074

Grant, S. B., Gomez-Velez, J. D., & Ghisalberti, M. (2018b). Modeling the effects of turbulence on hyporheic exchange and local-to-global nutrient processing in streams. *Water Resources Research*, *54*(9), 5883–5889. https://doi.org/10.1029/2018wr023078

Grant, S. B., Gomez-Velez, J. D., Ghisalberti, M., Guymer, I., Boano, F., Roche, K., & Harvey, J. (2020). A one-dimensional model for turbulent mixing in the benthic biolayer of stream and coastal sediments. *Water Resources Research*, *56*(12), e2019WR026822. https://doi.org/10.1029/2019WR026822

Hardy, R. J., Best, J. L., Parsons, D. R., & Marjoribanks, T. I. (2016). On the evolution and form of coherent flow structures over a gravel bed: Insights from whole flow field visualization and measurement. *Journal of Geophysical Research: Earth Surface*, *121*(8), 1472–1493. https://doi.org/10.1002/2015jf003753

Harvey, J. W., Böhlke, J. K., Voytek, M. A., Scott, D., & Tobias, C. R. (2013). Hyporheic zone denitrification: Controls on effective reaction depth and contribution to whole-stream mass balance: Scaling hyporheic flow controls on stream denitrification. *Water Resources Research*, *49*(10), 6298–6316. https://doi.org/10.1002/wrcr.20492

Hunt, J., Wray, A., & Moin, P. (1988). *Eddies, streams and convergence zones in turbulent flows*. Center For Turbulence Research.

Jia, L. C., Zhu, Y. D., Jia, Y. X., Yuan, H. J., & Lee, C. B. (2017). Image pre-processing method for near-wall PIV measurements over moving curved interfaces. *Measurement Science and Technology*, *28*(3), 035201. https://doi.org/10.1088/1361-6501/aa574c

Jones, J., & Mulholland, P. (1999). *Streams and ground waters*. Academic Press.

Kähler, C. J., Scharnowski, S., & Cierpka, C. (2012). On the uncertainty of digital PIV and PTV near walls. *Experiments in Fluids*, *52*(6), 1641–1656. https://doi.org/10.1007/s00348-012-1307-3

Kaufman, M. H., Cardenas, M. B., Buttles, J., Kessler, A. J., & Cook, P. L. M. (2017). Hyporheic hot moments: Dissolved oxygen dynamics in the hyporheic zone in response to surface flow perturbations. *Water Resources Research*, *53*(8), 6642–6662. https://doi.org/10.1002/2016WR020296

Kim, T., Blois, G., Best, J. L., & Christensen, K. T. (2018). Experimental study of turbulent flow over and within cubically packed walls of spheres: Effects of topography, permeability and wall thickness. *International Journal of Heat and Fluid Flow*, *73*, 16–29. https://doi.org/10.1016/j.ijheatfluidflow.2018.06.004

Knapp, J. L. A., González-Pinzón, R., Drummond, J. D., Larsen, L. G., Cirpka, O. A., & Harvey, J. W. (2017). Tracer-based characterization of hyporheic exchange and benthic biolayers in streams. *Water Resources Research*, *53*(2), 1575–1594. https://doi.org/10.1002/2016WR019393

Kuwata, K., & Suga, K. (2017). Direct numerical simulation of turbulent over anisotropic porous media. *Journal of Fluid Mechanics*, *831*, 41–71. https://doi.org/10.1017/jfm.2017.619

Leonardi, A., Pokrajac, D., Roman, F., Zanello, F., & Armenio, V. (2018). Surface and subsurface contributions to the build-up of forces on bed particles. *Journal of Fluid Mechanics*, *851*, 558–572. https://doi.org/10.1017/jfm.2018.522

Li, A., Aubeneau, A. F., Bolster, D., Tank, J. L., & Packman, A. I. (2017). Covariation in patterns of turbulence-driven hyporheic flow and denitrification enhances reach-scale nitrogen removal. *Water Resources Research*, *53*(8), 6927–6944. https://doi.org/10.1002/2016WR019949

Li, A., Bernal, S., Kohler, B., Thomas, S. A., Martí, E., & Packman, A. I. (2021). Residence time in hyporheic bioactive layers explains nitrate uptake in streams. *Water Resources Research*, *57*(2), e2020WR027646. https://doi.org/10.1029/2020WR027646

Lian, Y., Dallmann, J., Sonin, B., Roche, K., Liu, W., Packman, A., & Wagner, G. (2019). Large eddy simulation of turbulent flow over and through a rough permeable bed. *Computers & Fluids*, *180*, 128–138. https://doi.org/10.1016/j.compfluid.2018.12.015

Manes, C., Pokrajac, D., McEwan, I., & Nikora, V. (2009). Turbulence structure of open channel flows over permeable and impermeable beds: A comparative study. *Physics of Fluids*, *21*(12), 125109. https://doi.org/10.1063/1.3276292

Manes, C., Pokrajac, D., Nikora, V., Ridolfi, L., & Poggi, D. (2011). Turbulent friction in flows over permeable walls. *Geophysical Research Letters*, *38*.

Maniatis, G., Hoey, T., Hodge, R., Rickenmann, D., & Badoux, A. (2020). Inertial drag and lift forces for coarse grains on rough alluvial beds measured using in-grain accelerometers. *Earth Surface Dynamics*, *8*(4), 1067–1099. https://doi.org/10.5194/esurf-8-1067-2020

McKnight, D., Runkel, R., Tate, C., Duff, J., & Moorhead, D. (2004). Inorganic n and p dynamics of Antarctic glacial meltwater streams as controlled by hyporheic exchange and benthic autotrophic communities. *Journal of the North American Benthological Society*, *23*(2), 1901–1921. https://doi.org/10.1899/0887-3593(2004)023<0171:inapdo>2.0.co;2

Meyer, K. E., Pederson, J. M., & Özcan, O. (2007). A turbulent jet in crossflow analysed with proper orthogonal decomposition. *Journal of Fluid Mechanics*, *583*, 199–227. https://doi.org/10.1017/S0022112007006143

Mittal, R., & Iaccarino, G. (2005). Immersed boundary methods. *Annual Review of Fluid Mechanics*, *37*(1), 239–261. https://doi.org/10.1146/annurev.fluid.37.061903.175743

Nagaoka, H., & Ohgaki, S. (1990). Mass transfer mechanism in a porous riverbed. *Water Research*, *24*(4), 417–425. https://doi.org/10.1016/0043-1354(90)90223-s

Newcomer Johnson, T., Kaushal, S., Mayer, P., Smith, R., & Sivirichi, G. (2016). Nutrient retention in restored streams and rivers: A global review and synthesis. *Water*, *8*(4), 116. https://doi.org/10.3390/w8040116

Nguyen, C. V., Nguyen, T. D., Wells, J. C., & Nakayama, A. (2010). Interfacial PIV to resolve flows in the vicinity of curved surfaces. *Experiments in Fluids*, *48*(4), 577–587. https://doi.org/10.1007/s00348-010-0824-1

Nicoud, F., & Ducros, F. (1999). Subgrid-scale stress modelling based on the square of the velocity gradient tensor. *Flow Turbulence and Combustion*, *62*(3), 183–200. https://doi.org/10.1023/a:1009995426001

Nikora, V., Ballio, F., Coleman, S., & Pokrajac, D. (2013). Spatially averaged flows over mobile rough beds: Definitions, averaging theorems, and conservation equations. *Journal of Hydraulic Engineering*, *139*(8), 803–811. https://doi.org/10.1061/(asce)hy.1943-7900.0000738

Nikora, V., Goring, D., McEwan, I., & Griffiths, G. (2001). Spatially averaged open-channel flow over rough bed. *Journal of Hydraulic Engineering*, *127*(2), 123–133. https://doi.org/10.1061/(asce)0733-9429(2001)127:2(123)

Nikora, V., McEwan, I., McLean, S., Coleman, S., Pokrajac, D., & Walters, R. (2007). Double-averaging concept for rough-bed open-channel and overland flows: Theoretical background. *Journal of Hydraulic Engineering*, *133*(8), 873–883. https://doi.org/10.1061/(asce)0733-9429(2007)133:8(873)

O'Connor, B. L., & Harvey, J. W. (2008). Scaling hyporheic exchange and its influence on biogeochemical reactions in aquatic ecosystems. *Water Resources Research*, *44*(12), W12423.

O'Connor, B. L., Harvey, J. W., & McPhillips, L. E. (2012). Thresholds of flow-induced bed disturbances and their effects on stream metabolism in an agricultural river. *Water Resources Research*, *48*(8), W08504. https://doi.org/10.1029/2011wr011488

Packman, A., & Brooks, N. (2001). Hyporheic exchange of solutes and colloids with moving bed forms. *Water Resources Research*, *37*(10), 2591–2605. https://doi.org/10.1029/2001wr000477

Packman, A., Salehin, M., & Zaramella, M. (2004). Hyporheic exchange with gravel beds: Basic hydrodynamic interactions and bedform-induced advective flows. *Journal of Hydraulic Engineering*, *130*(7), 647–656. https://doi.org/10.1061/(asce)0733-9429(2004)130:7(647)

Padhi, E., Dey, S., Desai, V. R., Penna, N., & Gaudio, R. (2019). Water-worked gravel bed: State-of-the-art review. *Water*, *11*(4). https://doi.org/10.3390/w11040694

Pedras, M. H., & de Lemos, M. J. S. (2001). Macroscopic turbulence modeling for incompressible flow through undeformable porous media. *International Journal of Heat and Mass Transfer*, *44*(6), 1081–1093. https://doi.org/10.1016/s0017-9310(00)00202-7

Pokrajac, D. (2007). *Momentum transfer between a free-surface turbulent flow and a turbulent flow within an underlying porous medium*. Publications of the Institute of Geophysics, Polish Academy of Sciences, E-7(401).

Pokrajac, D., Manes, C., & McEwan, I. (2007). Peculiar mean velocity profiles within a porous bed of an open channel. *Physics of Fluids*, *19*(9), 098109. https://doi.org/10.1063/1.2780193

Reidenbach, M. A., Limm, M., Hondzo, M., & Stacey, M. T. (2010). Effects of bed roughness on boundary layer mixing and mass flux across the sediment-water interface. *Water Resources Research*, *436*(7).

Roche, K. R., Blois, G. L., Best, J. L., Christensen, K. T., Aubeneau, A. F., & Packman, A. I. (2018). Turbulence links momentum and solute exchange in coarse-grained streambeds. *Water Resources Research*, *54*, 3225–3242. https://doi.org/10.1029/2017wr021992

Roche, K. R., Li, A., Bolster, D., Wagner, G. J., & Packman, A. I. (2019). Effects of turbulent hyporheic mixing on reach-scale transport. *Water Resources Research*. *55*, 3780–3795. https://doi.org/10.1029/2018wr023421

Schmeeckle, M. W. (2014). Numerical simulation of turbulence and sediment transport of medium sand. *Journal of Geophysical Research: Earth Surface*, *119*(6), 1240–1262. https://doi.org/10.1002/2013jf002911

Schneider, G. E., & Raw, M. J. (1987). Control volume finite-element method for heat transfer and fluid flow using colocated variables—1. Computational Procedure. *Numerical Heat Transfer Part A Applications*, *11*(4), 363–390. https://doi.org/10.1080/10407788708913560

Shen, G., Yuan, J., & Phanikumar, M. (2020). Direct numerical simulations of turbulence and hyporheic mixing near sediment-water interfaces. *Journal of Fluid Mechanics*. *892*, A20. https://doi.org/10.1017/jfm.2020.173

Sherman, T., Roche, K. R., Richter, D. H., Packman, A. I., & Bolster, D. (2019). A dual domain stochastic Lagrangian model for predicting transport in open channels with hyporheic exchange. *Advances in Water Resources*, *125*, 57–67. https://doi.org/10.1016/j.advwatres.2019.01.007

Sinha, S., Hardy, R. J., Blois, G., Best, J. L., & Smith, G. H. S. (2017). A numerical investigation into the importance of bed permeability on determining flow structures over river dunes. *Water Resources Research*, *53*(4), 3067–3086. https://doi.org/10.1002/2016wr019662

Slattery, J. C. (1999). *Advanced transport phenomena*. Cambridge University Press. https://doi.org/10.1017/CBO9780511800238

Stoesser, T., Frohlich, J., & Rodi, W. (2007). Turbulent open-channel flow over a permeable bed. *Proceedings of the 32st IAHR Congress, International Association for Hydro-Environment Engineering and Research*. Italy.

Sund, N. L., Bolster, D., & Dawson, C. (2015). Upscaling transport of a reacting solute through a periodically converging–diverging channel at pre-asymptotic times. *Journal of Contaminant Hydrology*, *182*, 1–15. https://doi.org/10.1016/j.jconhyd.2015.08.003

Thibodeaux, L. J., & Boyle, J. D. (1987). Bedform-generated convective transport in bottom sediment. *Nature*, *325*(6102), 341–343. https://doi.org/10.1038/325341a0

Tonina, D., & Buffington, J. M. (2009). Hyporheic exchange in mountain rivers I: Mechanics and environmental effects. *Geography Compass*, *3*(3), 1063–1086. https://doi.org/10.1111/j.1749-8198.2009.00226.x

Voermans, J. J., Ghisalberti, M., & Ivey, G. N. (2017). The variation of flow and turbulence across the sediment–water interface. *Journal of Fluid Mechanics*, *824*, 413–437. https://doi.org/10.1017/jfm.2017.345

Voermans, J. J., Ghisalberti, M., & Ivey, G. N. (2018). The hydrodynamic response of the sediment-water interface to coherent turbulent motions. *Geophysical Research Letters*, *45*(19), 10520–10527. https://doi.org/10.1029/2018gl079850

Vollmer, S., Ramos, F. d. l. S., Daebel, H., & Kühn, G. (2002). Micro scale exchange processes between surface and subsurface water. *Journal of Hydrology*, *269*, 3–10. https://doi.org/10.1016/s0022-1694(02)00190-7

Ward, A. S., & Packman, A. I. (2019). Advancing our predictive understanding of river corridor exchange. *WIREs Water*, *6*(1), e1327. https://doi.org/10.1002/wat2.1327

Whitaker, S. (1985). *Simple geometrical derivation of the spatial averaging theorem* (Vol. 19).

Whitaker, S. (1986). Flow in porous media I: A theoretical derivation of Darcy's law. *Transport in Porous Media*, *1*(1), 3–25. https://doi.org/10.1007/BF01036523

Whitaker, S. (1999). *The method of volume averaging*. https://doi.org/10.1007/978-94-017-3389-2

Withers, P., & Jarvie, H. (2008). Delivery and cycling of phosphorus in rivers: A review. *The Science of the Total Environment*, *400*, 379–395. https://doi.org/10.1016/j.scitotenv.2008.08.002

Xia, X., Zhang, S., Li, S., Zhang, L., Wang, G., Zhang, L., et al. (2018). The cycle of nitrogen in river systems: Sources, transformation, and flux. *Environmental Science: Processes & Impacts*, *20*, 863–891. https://doi.org/10.1039/C8EM00042E

Yang, J. Q., & Nepf, H. M. (2018). A turbulence-based bed-load transport model for bare and vegetated channels. *Geophysical Research Letters*, *45*(19), 10428–10436. https://doi.org/10.1029/2018GL079319

Zheng, L., Cardenas, M. B., Wang, L., & Mohrig, D. (2019). Ripple effects: Bed form morphodynamics cascading into hyporheic zone biogeochemistry. *Water Resources Research*, *55*(8), 7320–7342. https://doi.org/10.1029/2018WR023517